Multi-scale Molecular Imaging of Human Cells reveals COPI and COPII Vesicles at ER Exit Sites

Katie Downes[1,2], Julia Flood[3], Andrea Nans[4], Sander Van der Verren[2,5,6], Anjon Audhya[3], Giulia Zanetti[1,2,5]*

1. Institute of Structural and Molecular Biology, University College London, WC1E 6BT, UK.
2. The Francis Crick Institute, London, NW1 1AT, UK.
3. Department of Biomolecular Chemistry, University of Wisconsin School of Medicine and Public Health, Madison, WI, 53706, USA
4. Structural Biology Science Technology Platform, The Francis Crick Institute, London, NW1 1AT, UK.
5. Institute of Structural and Molecular Biology, Birkbeck College London, WC1E 7HX, UK
6. Current address: Department of Plant Biotechnology and Bioinformatics, Ghent University - Center for Plant Systems Biology, Flemish Institute for Biotechnology, 9052 Ghent, Belgium

*correspondence: g.zanetti@bbk.ac.uk, giulia.zanetti@crick.ac.uk

Abstract:

Trafficking from the endoplasmic reticulum to the Golgi apparatus comprises the first steps toward the correct localization of 30% of eukaryotic proteins. Coat protein complexes COPII and COPI are involved in forward and retrograde transport of cargo and cargo receptors between the ER and the Golgi. Although COPII forms coated vesicles in vitro, the biogenesis, morphology and organization of transport carriers in mammalian cells is debated. We use in situ cryo-electron tomography and super-resolution fluorescence microscopy to reveal the molecular architecture of ER exit sites in human cells. We visualise ribosome-exclusion zones enriched with COPII and COPI-coated vesicles and thus resolve the debate regarding the existence of COPII coated vesicles. COPII vesicles derive from ER membranes, whereas COPI vesicles originate from the ER-Golgi intermediate compartment. We quantify coated vesicle morphology and positioning with respect to other ER exit site components, providing a molecular description of the mammalian early secretory pathway.

Introduction:

The secretory pathway is responsible for the delivery of approximately 30% of eukaryotic proteins to their functional locations, including the majority of membrane and secreted proteins. Many of its components are essential and highly conserved, and pathological mutations impacting the secretory pathway result in the mis-trafficking of proteins, leading to a variety of human disorders.

Despite their importance, many of the molecular mechanisms that regulate protein secretion are poorly understood[1,2].

The secretory pathway starts with the transport of newly synthetized proteins from the endoplasmic reticulum (ER) to the Golgi apparatus, where they acquire posttranslational modifications and are sorted. ER exit occurs at specific subdomains of the ER, called transitional ER, which in most organisms appear as punctate structures when fluorescently labelled via their stable components[3].

In mammalian cells, where the Golgi is often concentrated in the perinuclear region, the ER-Golgi intermediate compartment (ERGIC) sits between sites of transitional ER and the cis-Golgi[3]. The transitional ER-ERGIC interfaces, commonly referred to as ER exit sites (ERESs), are found across the whole cell volume and are characterized by ribosome-free areas enriched with vesicular tubular membranes[4]. ERESs proximally positioned to cis-Golgi cisternae enable rapid cargo transit through the early secretory pathway, whereas cargo from peripheral ERESs traverse the cytoplasm towards the Golgi via mobile ERGIC compartments[5,6]. The mechanistic underpinnings driving ERGIC function, traffic and morphogenesis remain unknown.

ER exit is dependent on a set of cytosolic proteins that together form the coat protein complex II (COPII)[1]. According to the prevalent model, born from early observations of membrane vesicles near the Golgi of secretory cells[4,7] and supported by decades of biochemical and structural studies[8–15], COPII assembles at transitional ER to form a coat that remodels the membrane into 60-100 nm vesicles, while simultaneously recruiting cargo proteins into the budding carriers. Upon uncoating, carriers fuse with target ERGIC membranes to release their cargo. Cargo receptors and adaptors, together with escaped ER resident proteins, are retrieved from either the ERGIC or cis-Golgi and transported back to the ER via retrograde vesicular transport mediated by the coat protein complex I (COPI)[16,17], which is recruited to ERESs and has been shown to act sequentially to COPII[18–20].

COPII and COPI membrane budding reactions have been reconstituted in vitro using purified coat components to reveal the molecular mechanisms of coat assembly and membrane remodeling [9,12,21–23]. During COPII-mediated ER exit, the small GTPase Sar1 is activated by the ER-resident guanine nucleotide exchange factor (GEF), Sec12[24]. Upon activation, Sar1 stably inserts its amino-terminal amphipathic helix into the ER membrane and recruits the inner layer of the coat, comprised of Sec23-Sec24 heterodimers[25]. Sec24 is mainly responsible for recognition of cargo and cargo receptors[14], while Sec23 recruits the outer layer of the COPII coat, made of rod-shaped Sec13-Sec31 heterotetramers that assemble to form cage-like structures[12,13,25]. Polymerization of both the inner and outer coat contribute to generating and regulating membrane curvature[12]. COPII coated vesicles are selectively transported to the ERGIC, in a manner regulated by condensates of TRK-fused gene protein (TFG) in mammalian cells, where they fuse to deliver their cargo[26]. Coat disassembly is facilitated by Sec23, which functions as a guanine nucleotide activating protein (GAP) for Sar1[25,27], and is further stimulated by Sec31. However, the timing and regulation of the uncoating process remain unknown.

In the case of COPI, the small ribosylation factor Arf1 is activated by dedicated GEFs. Arf1 then inserts its myristoylated amino-terminus into Golgi or ERGIC membranes and recruits the 7-membered coatomer complex (formed by subunits $\alpha, \beta, \beta', \gamma, \delta, \varepsilon,$ and ζ), en-bloc[16,17,28,29]. Coatomer polymerization is coupled with the induction of membrane curvature, while cargo binding is orchestrated by the β and δ-COP subunits[16]. Two copies of ArfGAP are recruited by each coatomer, inducing stepwise GTP hydrolysis that initially enhances cargo recruitment and eventually leads to coat disassembly. It is likely that residual COPI coat subunits on the vesicle membrane promote tethering to target membranes[16].

Although COPII and COPI-coated vesicles have been visualized at ERESs in situ by cryo-EM analysis of green algae[30], direct evidence for this two-way vesicular transport system in vertebrates is lacking. Recent technological advances in high-resolution and live cell fluorescence microscopy have introduced doubts that the 'classical' vesicular model represents the main mechanism of COPII-mediated ER exit in higher eukaryotes. Live cell imaging showed that the majority of COPII does not move from its steady state location in human cells, whilst COPI is seen moving with ERGIC membranes to the Golgi[6,31]. Moreover, volume EM of ERESs has shown what appear to be clusters of tubular vesicular membranes stably connected to the ER in COPII-positive regions, with COPI-positive tubules emanating from them, giving rise to the idea that COPII might form a collar to act as a 'gate-keeper' rather than a coat at human ERESs[5].

The quest to discover ER exit mechanisms beyond the classic small vesicles model stems from the difficulty of explaining transport of the diverse range of cargo that are secreted in vertebrates, which include abundant and large proteins such as lipoproteins, collagens, and other extracellular matrix components[1,32,33].

Here, we sought to map the molecular organization of the early secretory pathway in human epithelial cells, with the aim to resolve controversies regarding the mechanisms of protein transport, and to provide a molecular-level understanding of the interplay between COPII, COPI, and other components of ERESs.

We used cryo-correlative light and electron microscopy (cryo-CLEM) on unperturbed human retinal pigment epithelial (RPE-1) cells to target ERESs for cryo-focused ion beam milling scanning electron microscopy (cryo-FIB/SEM) and acquire cryo-electron tomography (cryo-ET) datasets. We were able to unambiguously resolve the COPII and COPI coats on membrane vesicles and buds. We also used stimulated emission depletion (STED) and high-resolution confocal fluorescence imaging to quantify the relative positioning of ERES components. All together we provide a molecular description of ERESs in human cells and our results clearly and unambiguously support the vesicular transport model.

Results:

Identification of ERESs in situ

Typical mammalian cells contain a few hundred ERESs, as seen by fluorescence microscopy (Supplementary Figure 1A,B). Given the limited volume that can be imaged via cryo-ET of FIB-milled lamellae (typically below 0.5 μm^3), the probability of encountering an ERES by random milling and acquisition is on the order of 1 in 100, effectively impairing our ability to unequivocally localise ERESs and obtain non-ambiguous datasets containing our target of interest. To improve targeting of ERESs, we adopted a cryo-CLEM approach, making use of previously established human epithelial cells that express a functionally tagged version of Sec23A at its endogenous locus[34].

Briefly, CRISPR-Cas9 editing was used to create a translational fusion between HaloTag and the dominant Sec23 paralog SEC23A at its endogenous locus in RPE-1 cells, resulting in a homozygously edited line. Depletion of Sec23B in the edited cell line did not impair growth nor viability, and movement of secretory cargo was unaffected, indicating the tagged Sec23A is functional[34]. Immunofluorescence experiments support this finding as HaloTag-Sec23A colocalizes with other components of the COPII coat (Supplementary Figure 1C), which show a similar intracellular distribution when compared to unedited, control cells (Supplementary Figure 1A). The HaloTag-Sec23A RPE-1 cell line was therefore identified as a suitable system for investigating native ERES structure.

The ligand Oregon Green-HaloTag was used to visualize HaloTag-Sec23A under cryo-conditions using the integrative fluorescence light microscope (iFLM) module of the Aquilos 2 FIB/SEM (Supplementary Figure 1D). Clusters of fluorescent puncta were targeted for FIB milling to increase the likelihood of the target remaining in the final lamella. Post thinning, the fluorescence signal of the lamella was checked to confirm successful targeting (Supplementary Figure 1D, right panel and Supplementary Figure 2A,F).

Transmission EM (TEM) search maps of each lamella were acquired and overlaid with the lamella fluorescence to guide cryo-ET acquisition at 2.24 Å/pixel. This small pixel size was chosen to maintain the potential to perform subtomogram averaging and resolve complexes in situ at molecular resolution. However, difficulties in aligning the fluorescence data from the iFLM and TEM search maps often led to inaccurate positioning of tilt-series acquisition sites. Given that the structure of an ERES has no discernible features visible in the TEM search maps (Supplementary Figure 2B,C,G,H) combined with the small field of view (~900 nm X 900 nm), sites of interest were easily missed. With this pipeline we achieved a 7% success rate of targeting ERESs (30 tomograms that contained ERESs out of 410).

To further improve targeting success, we included a novel intermediate step (Supplementary figure 2D). A high defocus, low dose, restricted tilt series was acquired at a larger pixel size of 7.27 Å/pix at sites of fluorescence. On the fly processing allowed 3D reconstructions to be quickly generated. Despite accumulating less than 10 electrons/$Å^2$, the resulting tomograms were of suitable clarity

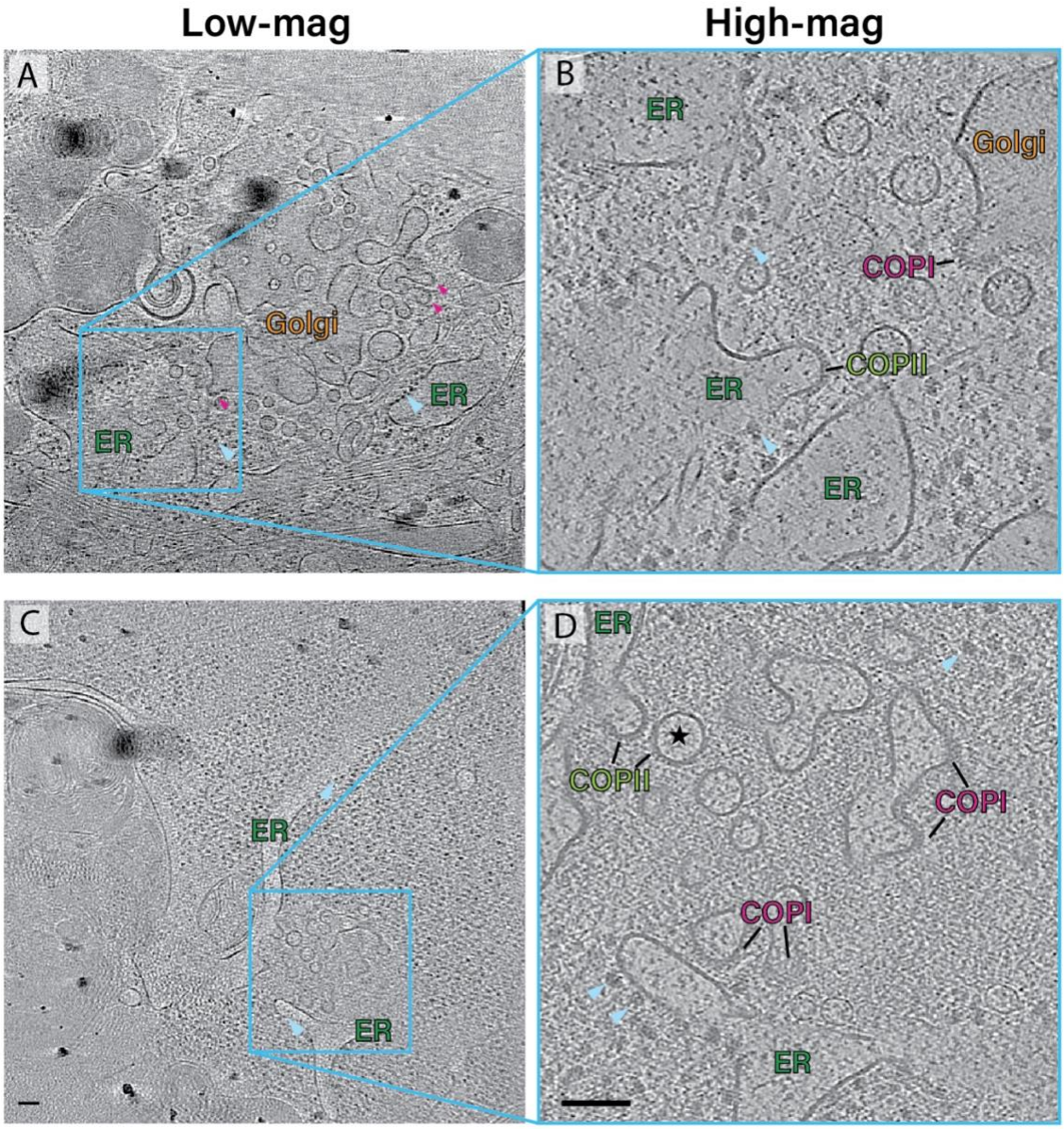

Figure 1

Cryo-ET of ERESs in HaloTag-Sec23A RPE-1 cells.

A. *Slice through the xy plane of a reconstructed tomogram from a high-defocus, low-magnification tilt series from a FIB/SEM lamella of HaloTag-Sec23A RPE-1 cells, providing a panoramic view of cellular features. The ER is studded with ribosomes (pale blue arrowheads), while Golgi cisternae appear fenestrated and enriched with coated vesicles (purple arrowheads).*
B. *Slice through the xy plane of a reconstructed tomogram from a high-magnification tilt series collected in the area highlighted in the cyan box in A, acquired at a resolution where molecular features such as COPII and COPI-coated membranes become apparent.*
C. *As in A, but from a different lamella where no Golgi apparatus is visible.*
D. *As in B.*

Scale bars 100 nm.

and contrast to identify various intracellular structures, including small membrane buds and vesicles (Figure 1A,C). Informed by this low-magnification 3D data, we selected potential regions of interest for high-magnification data collection at 2.24 Å/pixel. These were chosen based on the presence of vesicular or tubular membranes in the vicinity of the endoplasmic reticulum, which was easily identified by its decoration with ribosomes (Supplementary Figure 2E,J and Figure 1B,D).

Using this pipeline, we identified 134 regions of interest for high-magnification data collection, of which 28% clearly contained clusters of ER-derived coated vesicles and buds, a 4-fold improvement to that achieved before. The remaining 72% contained membrane structures that did not appear coated or were not ER-associated and therefore were not analyzed further.

Optimization of tilt series alignment

To improve tilt series alignment and validate the tomogram information content, we performed subtomogram averaging of ribosome particles. We picked over 16,000 ribosomes using a template matching routine (Supplementary Figure 3A,B). Ribosomes were subjected to subtomogram averaging following the WARP, relion, and M pipeline[35] and gave rise to a subtomogram averaged map at 15 Å resolution (Supplementary Figure 3C-F,I).

To control for template bias, ribosome alignments were repeated with references that had mirrored handedness. The relion refined map spontaneously reverted to the same structure we obtained previously (albeit with a different overall orientation), confirming that the refinements are not affected by bias from the original template used during picking. This also allowed us to unambiguously assign the correct handedness to our reconstructed tomograms (Supplementary Figure 3G,H). In addition to tilt series alignment optimization and validation of the resolution and handedness of our reconstruction, this exercise also provides us with 3D distribution maps of ribosomes, which allows us to define ribosome exclusion zones.

Identification of COPII and COPI coats

Inspection of the optimized high magnification tomograms allows detection of vesicle coats. Comparison to coat density seen in previous in vitro reconstitution cryo-ET work allows COPII and COPI to be visually identified (Figure 2A-C). Whereas COPI consists of a thick, fuzzy layer around the membrane (Figure 2B), COPII has a well-defined, thinner inner coat layer, and a sparser outer layer (Figure 2A). The outer layer was only visible in some slices in our in situ data, due to its long and thin structure which tends to be buried in the background of cytosolic components.

We sought unbiased confirmation of our manual coat assignment via template matching. Using a semi-automated membrane segmentation routine, we created loose masks around all coated membranes (Supplementary Figure 4) and searched masked tomograms using available COPI or COPII structures as templates (EMD-3968 and EMD-19417, respectively). Both templates were run against identical masked tomograms. When we visualized the highest cross-correlation peaks from the template matching, there was clear discrimination of the two classes of coat, with the COPII

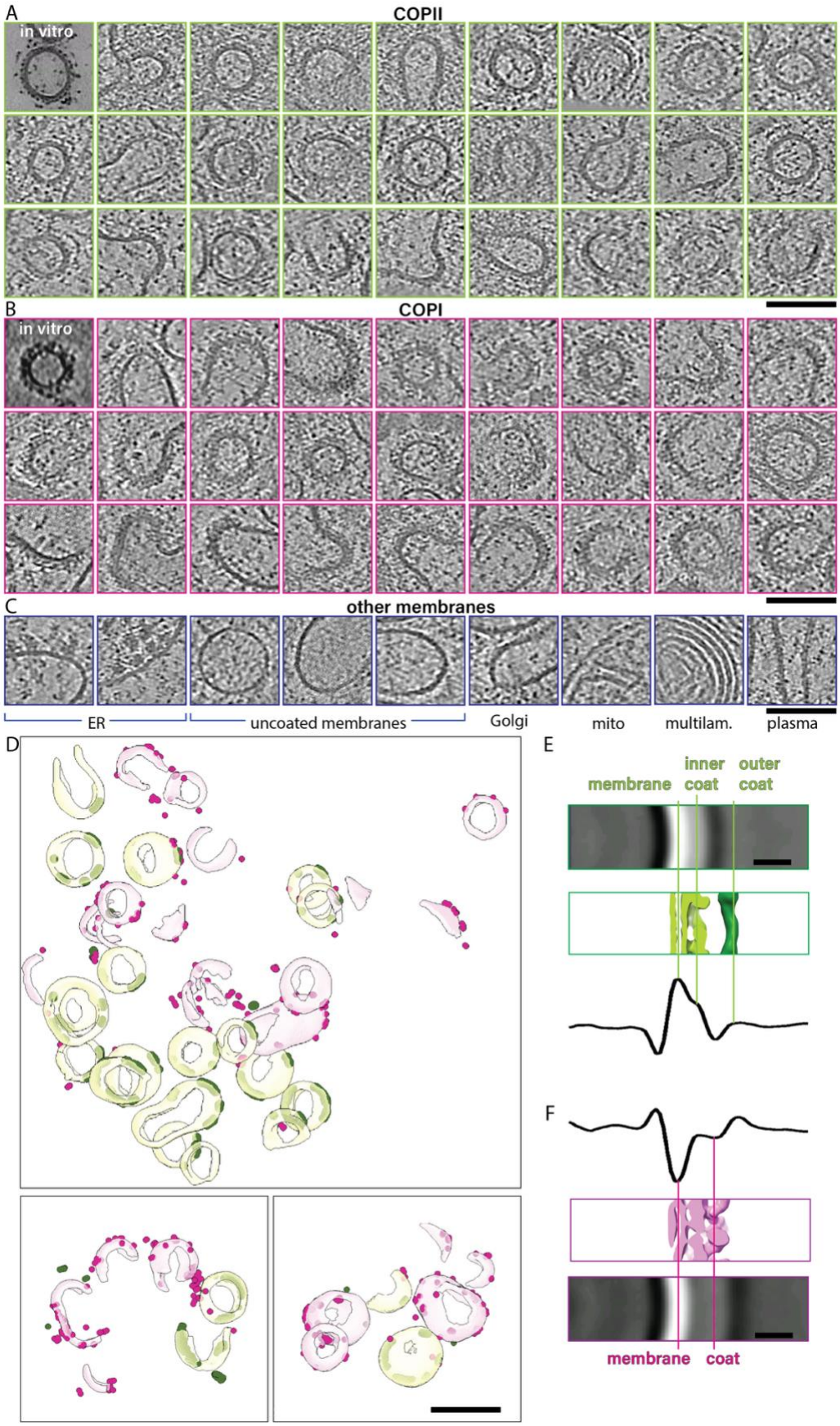

emplate Figure

Figure 2

Identification of COPII and COPI-coated vesicles.

A. *Gallery of xy slices through COPII-coated vesicles from cryo-lamellae. Top-left panel shows an in vitro reconstituted vesicle for comparison*[12].
B. *Gallery of xy slices through COPI-coated vesicles from cryo-lamellae. Top-left panel shows an in vitro reconstituted vesicle for comparison*[23].
C. *Gallery of xy slices through other classes of membranes, as described below each panel.*
D. *3D rendering of segmented coated membranes are shown in pale green and purple depending on whether they were manually assigned to COPII or COPI respectively. The highest cross-correlation peaks upon template matching using EMD-3968 as template (COPI structure) are shown as pink spheres, and those obtained with EMD-19417 as template (COPII structure) are shown in green. Template matching discriminates between the two classes of vesicles and there is very good agreement with our previous manual assignment. Three exemplary tomograms are shown.*
E. *Top: Slice through the yz plane of the subtomogram average of particles picked from random oversampling of COPII-coated membranes, oriented normal to the membrane, and aligned via shifts only. Middle: the profile of an in vitro reconstituted sample is shown for comparison. Bottom, density profile obtained from the top panel.*
F. *As in E, but for COPI. Panels are mirrored for clarity of comparison.*

Scale bars: A-D 100 nm, E-F 10 nm.

template preferably matching coated membranes that we previously identified as COPII, and vice versa (Figure 2D, Movie 1). The templates for both COPI and COPII were matched in positions and orientations that are consistent with the membrane curvature, further validating the peaks as true positives (Supplementary Figure 4A,B,D,E). As a control, we performed template matching against a randomly masked tomogram which yielded disordered matched templates (Supplementary Figure 4C,F), giving us confidence in our assignments.

We extracted COPI and COPII particles by randomly and evenly sampling corresponding coated membranes, assigned yaw and pitch angles normal to the membrane, and randomized their in-plane rotation. Upon 5 iterations of shift-only alignment and averaging we traced the density profile for each coat (Figure 2E,F). For COPII, the profile was characterized by an intense double peak, and a weaker distal peak (Figure 2E). This arrangement is consistent with the primary peak being formed by the membrane bilayer and the tightly juxtaposed inner coat, and the secondary peak resulting from the sparser outer coat, as reported previously in structures determined from in vitro budding reconstitution using yeast proteins[11,12,36]. This suggests that the coat architecture described previously at high resolution is likely to be physiologically relevant. A similar result was obtained for COPI (Figure 2F), where the average profile is consistent with the presence of a single ~50 Å thick coat layer immediately juxtaposed to the membrane bilayer, as described in reconstitution experiments performed previously with mouse proteins and in situ studies of the green alga Chlamydomonas reinhardtii [22,30].

The Ultrastructure of ERESs – COPII and COPI vesicles

With confidence in our assignment of coat identity, we were able to qualitatively and quantitatively characterize the molecular ultrastructure of ERESs in 63 COPII-containing cryo-tomograms.

COPII coated vesicles appear clustered in ribosome-free regions of the cytosol, occupying areas with diameters ranging from ~150 to 700 nm. The ribosome exclusion zone showed no immediately obvious difference in electron density compared to the rest of the cytoplasm and did not appear to display a gradual decrease in ribosome density, but rather a sharp cut off (Figure 3).

COPII coated membranes were observed either budding from regions of ER, or as free vesicles in close proximity to, but clearly separated from, the ER membrane (Figure 3). We note that the thickness of our tomograms (150-350 nm) allows for full vesicles to be resolved, leaving no ambiguity as to whether these are truly vesicles or sections through a tube. To confirm the displacement of COPII coated vesicles from their origin ER membranes we used high-resolution confocal fluorescence microscopy, taking advantage of the scaffolding protein Sec16A as the marker for transitional ER. We imaged edited RPE-1 cells expressing HaloTag-Sec23A stained with JFX650-HaloTag ligand and anti-Sec16 antibodies, which appeared partially overlapping (Figure 4A). Quantification of the displacement between transitional ER and COPII, revealed an average distance of 90 nm within a 0 to 200 nm range, consistent with our cryo-EM observations (Figure 4B).

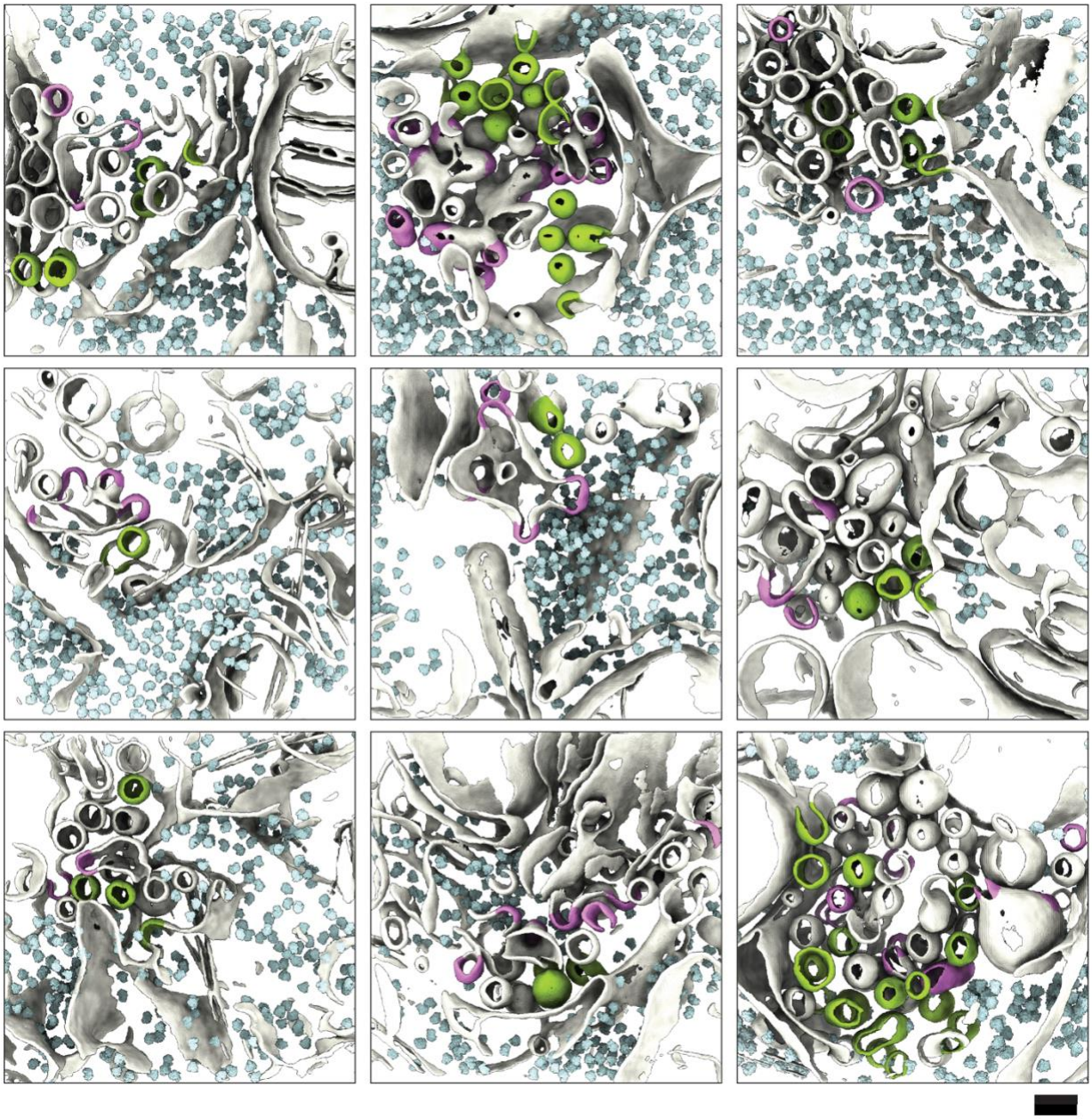

Figure 3

Molecular organization of ERESs.

A gallery of 3D rendered segmented tomograms of ERESs, where membranes are white, COPII-coated membranes are green, COPI-coated membranes are purple, and ribosomes are pale cyan. Scale bar 100 nm.

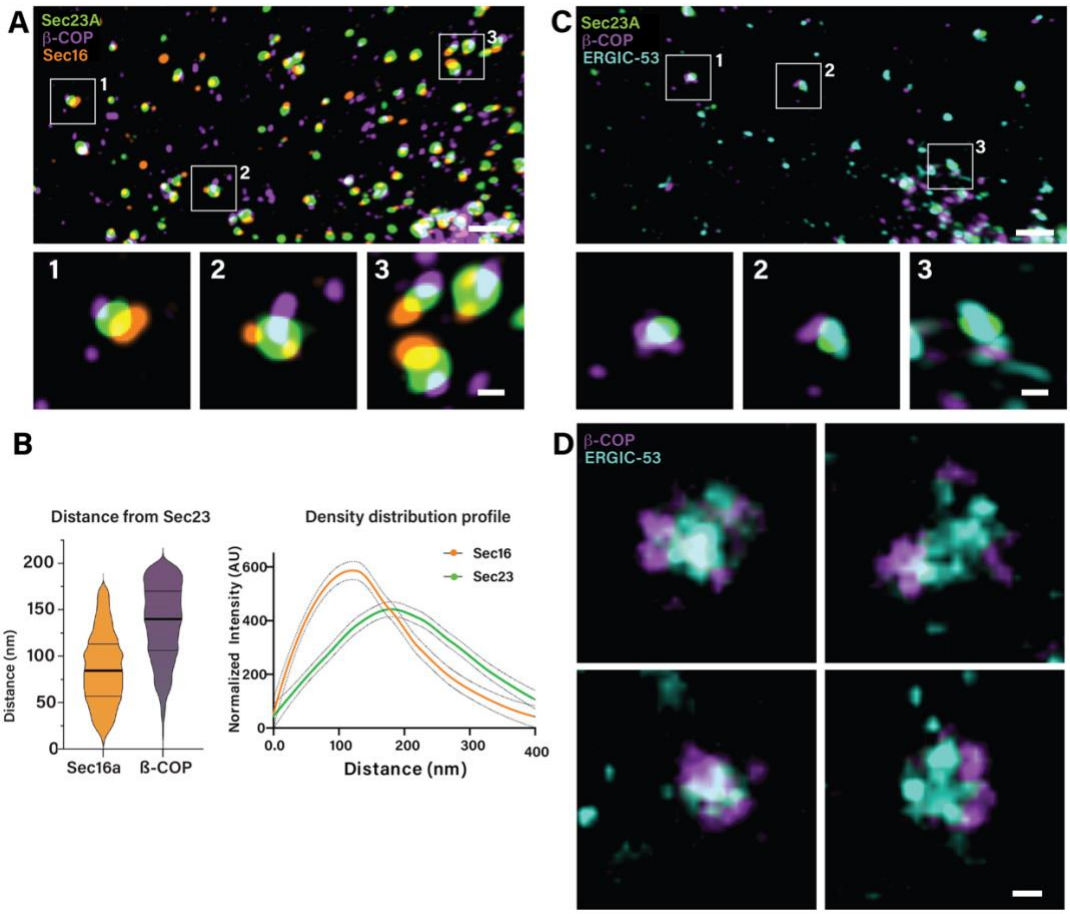

Figure 4

Fluorescence imaging of ERES components.

A. *Three-colour high resolution confocal fluorescence imaging of endogenous HaloTag-Sec23A RPE1 cells dyed with HaloTag JFX650 ligand (green) and stained with antibodies directed against Sec16 (orange) and β-COP (purple).*
B. *Quantitative data highlighting the relative distribution of COPII (HaloTag-Sec23A) and transitional ER (Sec16A). Left panel: Violin plots of the distance between centroids of endogenous HaloTag-Sec23A puncta from immunostained Sec16 and β-COP. Extracted from the three-color high resolution confocal fluorescence imaging as exampled in A. For Sec16, n = 5819, from ≥10 cells, across 3 experimental repeats. For β-COP, n = 4950, from ≥10 cells, across 4 experimental repeats. Right panel: Averaged linescans of Sec16 (orange) and HaloTag-Sec23A (green), extracted from two-colour super resolution STED imaging and fitted from 50 structures across 2 cells over 1 experimental repeat. Standard error is shown by the dotted lines. The intensity values were normalized for display purposes.*
C. *Three-color high resolution confocal fluorescence imaging of endogenous HaloTag-Sec23A RPE1 cells dyed with HaloTag JFX650 ligand (green) and stained with antibodies directed against ERGIC-53 (cyan) and β-COP (purple).*
D. *Two-colour super resolution STED imaging of endogenous SNAP-tag-ERGIC-53 RPE1 cells stained with antibodies directed against β-COP (purple) and SNAP-tag-ERGIC-53 dyed with JFX650-SNAP-tag ligand (cyan)*

Scale bar: A,C overviews: 1 µm, insets: 200 nm, D: 100 nm

COPI coated structures were found in close proximity to COPII coated membranes in 86% of the tomograms, with only 14% of COPII-containing tomograms not showing evidence of COPI coated membranes. Of the latter, we cannot establish whether COPI is present in the vicinity of COPII but is excluded from the field of view, or truly absent. Using 3-color high resolution confocal imaging, we found COPI near almost all Sec23A puncta, at an average distance of 134 nm and often on the distal side from Sec16A (Figure 4A,B). 77% of COPI puncta were not associated with COPII puncta and most likely represent Golgi-derived COPI vesicle clusters. We note that many tomograms in the full cryo-ET dataset contain COPI but not COPII coated vesicles. However, we did not include these in our analysis as there is no evidence to suggest that these vesicles are associated with ERESs, as opposed to the Golgi.

Unlike COPII, ERES-localized COPI coated buds extend from membranous vesicular-tubular clusters distinct from the ER (Figure 3). Previous studies have shown the co-localization of COPI and the ERGIC marker ERGIC-53[37]. We used high resolution confocal fluorescence imaging to assess the relative position of COPI, COPII and ERGIC-53 in our cells, confirming the tight juxtaposition of both COPI and COPII with ERGIC-53 (Figure 4C). Super resolution 2-color STED of endogenously tagged ERGIC-53 RPE-1 cells further showed that COPI vesicles were tightly co-localized with ERGIC-53 puncta and often appeared to encircle them (Figure 4D). These data strongly suggest that the compartments from which we observe COPI vesicles originating are ERGIC membranes.

The number of COPII coated membranes observed in cryo-tomograms of ERESs, inclusive of buds and vesicles, varies from 1 to 19 per ERES, with most ERESs having 1-3 COPII events (Figure 5A). The number of COPI events at ERESs varied between 0 and 21 with the majority containing 1-3 COPI structures (Figure 5B). We note this is likely an underestimation as the overall size of an ERES in 3 dimensions will often exceed the thickness of the tomogram by 2-3 fold. On average, from our ERES-containing tomograms, there were more COPI than COPII events per ERES. However, due to the proximity of the Golgi in several tomograms, it is often impossible to know whether the COPI vesicles were ERGIC or Golgi-derived, leading to a potential overestimation of their number. Nevertheless, we detected a significant positive correlation between the number of COPII and COPI events at each ERES ($R=0.53$, $P=1.5E-9$), indicating their functional and/or morphogenetical interdependence (Figure 5C).

Non-coated vesicles and non-coated pleomorphic structures were also observed within the ribosome exclusion zone and near both COPII and COPI vesicles (Figure 3). Occasionally, partially coated COPII vesicles were seen, further corroborating the hypothesis that uncoating happens before fusion (see for example black star in Figure 1D). However, such events are hard to quantify due to the high noise levels associated with in situ data, the fact that some vesicles are only partially contained in the tomogram volume, and the anisotropy of the reconstruction. Whether uncoated membranes are mechanistically involved in ERES function is unknown, but it is plausible they represent previously coated structures, which act as fusion competent intermediates.

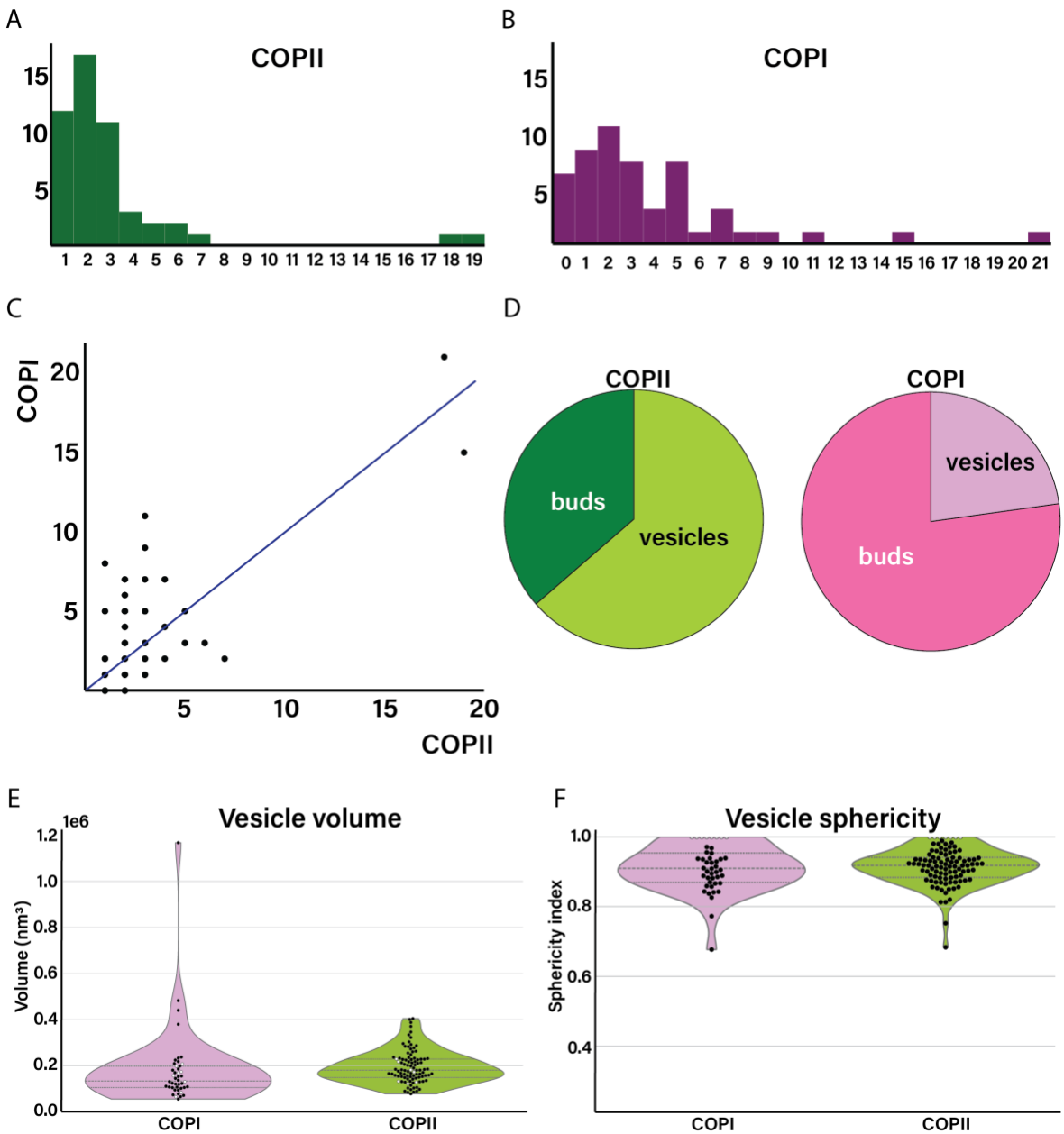

Figure 5

Morphometric analysis of coated membranes.

A. Distribution of the number of COPII-coated events per ERES.
B. Distribution of the number of COPI-coated events per ERES.
C. Scatter plot of the number of COPI vs COPII coated events. The blue solid line represents x=y.
D. Pie chart showing the relative abundance of buds vs vesicles for COPII (green) and COPI (purple).
E. Violin plot showing the volume distribution of all COPI and COPII-coated vesicles.
F. Violin plot showing the sphericity of all COPI and COPII-coated vesicles.

White and black circles indicate vesicles best fitted by a sphere and ellipsoid respectively. Dashed and dotted grey lines indicate the median and interquartile range respectively.

Transport Carrier Morphology at ERESs

As described above, we detected fully detached coated vesicles as well as coated membrane buds (Figure 3 and Figure 6). COPII buds were always associated with ER membranes, whereas COPI buds were always associated with ERGIC or Golgi membranes. This suggests that, for both COPII and COPI, we detect budding events, rather than fusion events. We never saw uncoated buds associated with either ER or ERGIC membranes, indicating that in both cases, uncoating occurs after scission, but before fusion with the target compartment, and that potential fusion events of transport vesicles are rapid and unlikely to be detected in tomograms. COPII appears to be more often associated with detached free vesicles than COPI (Figure 5D), suggesting scission and uncoating occur over distinct timescales for the two coats.

We performed morphometric analysis[38] to fit the segmented and extracted coated membranes to ellipsoids and spheres and determined which shape best described each structure to quantify their volume and sphericity. Most COPI and COPII coated vesicles were best described by the ellipsoidal fit, assessed by the root mean square error (RMSE) of the fit (Supplementary Figure 5A).

COPII coated vesicles have a median volume of 180,760 nm^3 (Figure 5E), which when approximated to a sphere corresponds to a diameter of 70 nm, consistent with previous reports[8,9,12]. The COPII coated vesicle volumes ranged from 78,007 nm^3 to ~400,000 nm^3 (Figure 5E), corresponding to approximated spheres with diameters of 53.3 nm and 91 nm respectively.

COPI coated vesicles have a significantly smaller median volume of 134,153 nm^3 (P=0.0014, Figure 5E), which corresponds to a sphere with a diameter of 64 nm. This is slightly larger than previously reported for both in situ Chlamydomonas vesicles and vesicles reconstituted in vitro with mouse proteins, which have mean diameter of ~55 nm[23,30]. However, this previously reported volume is included within the range observed in this dataset (Figure 5E), which corresponds to a spherical diameter of 47 nm to 131 nm. Our measurements therefore suggest there may be morphological differences in COPI coated vesicles between different species.

The distributions of the volume of COPI and COPII vesicles are also significantly different (P=0.0014), with COPI displaying a greater overall range and a pronounced positive tail (Figure 5E). This suggests that the COPI machinery may tolerate a greater range in carrier size whereas COPII may allow less flexibility.

Morphological analysis of budding membranes still attached to the donor compartment was more challenging than vesicles, due to the range of morphologies present in the data and the presence of an 'open face' (Supplementary Figure 5B). Nevertheless, ellipsoids and spheres can still be used to approximate their encompassed volume. To this end the 149 COPI and 56 COPII coated buds present in our data were extracted and analyzed. COPII coated buds enclosed volumes ranging from 32,229 nm^3 to 782,226 nm^3 with a median of 158,885 nm^3 (Supplementary Figure 5C), which correspond to a spherical diameter of 39 nm, 144 nm and 67 nm respectively. COPI coated buds were not significantly different than COPII in terms of both scale and distribution and ranged from

5,560 nm^3 to 3,215,442 nm^3 with a median of 141,587 nm^3 (Supplementary Figure 5C), corresponding to a spherical diameter of 22 nm, 183 nm and 65 nm respectively.

We calculated the ratio between the shortest and longest elliptical axis to measure vesicle sphericity. There was no significant difference in sphericity index between COPI and COPII vesicles. Both coated vesicles range from ~0.7 – 1 with a median of ~0.9 (Figure 5F) showing that both types of coated vesicles tend to be close-to-spherical in shape.

The Ultrastructure of ERESs – cellular context

Analysis of pairs of high and low-magnification tomograms provide detailed intracellular context. Golgi membranes can be identified in both high and low-magnification tomograms (Figure 1A,B and Figure 6) and thus the spatial relationship between ERESs, ERGIC and Golgi can be extracted. In some cases, ERESs were observed in close proximity to characteristic Golgi membranes allowing their classification as central or perinuclear ERESs, whilst others are distant from any visible Golgi (Figure 1A,C and Figure 6). While we can't exclude that Golgi may have been removed by FIB milling, proximity to the plasma membrane allows us to characterize some of these as peripheral ERESs (Figure 6, bottom). ERGIC membranes, characterized by their vesicular tubular morphology and COPI-coated buds, were observed indiscriminately at both peripheral and centrally located ERESs (Figure 6).

When ERESs are only a few hundred nanometers away from Golgi membranes, it can be hard to distinguish the ERGIC from the cis-Golgi cisterna. However, such distinction might be a matter of definition in a context where the ERGIC matures to become cis-Golgi.

It is unclear whether and to what extent COPI and COPII coated vesicles rely on cytoskeletal filaments for their directed movement. We analyzed our tomograms for the presence of filaments and found a great degree of heterogeneity. 72% of ERES tomograms contained microtubules (numbering between 1 and 4), but these didn't appear preferentially associated with any of the membranes involved. 84% contained intermediate filaments, often forming an extended meshwork encompassing the entire ERES area. Finally, actin was observed in 17% of tomograms. In all cases, no significant difference was found in the frequency of filaments in tomograms with or without ERESs (P=0.825 for microtubules, P=0.317 for intermediate filaments and P=1 for actin filaments), and thus a role for filaments specific to ERESs cannot be envisaged or established.

TFG tethers COPII vesicles at ERESs

Condensates composed of TFG have been shown to cluster COPII transport intermediates at ERESs, contributing to their uncoating via competition with outer coat component Sec31[39–42]. High-resolution confocal fluorescence imaging confirmed that TFG co-localizes with HaloTag-Sec23A (Figure 7A), and closely juxtaposes to other ERES components, including Sec12 (Figure 7A). Recent studies suggest that TFG condensates may act as a sieve, enabling entry of COPII coat proteins but not assembled COPI[43]. However, the interspersed distributions of COPII- and COPI-coated membranes seen by cryo-ET is inconsistent with the existence of a TFG barrier separating the two

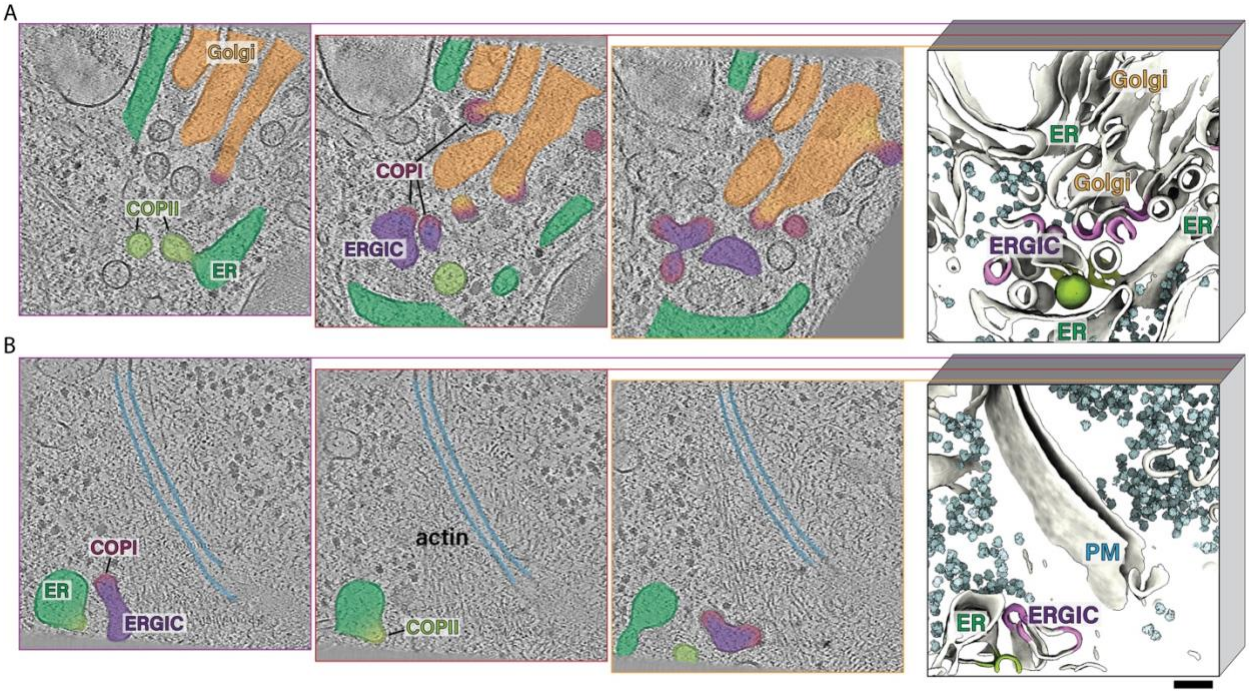

Figure 6

Perinuclear and peripheral ERESs.

A. Left: three xy slices through different z planes of a reconstructed high-magnification tomogram (3D-rendered as in Figure 3 on the right). Features have been coloured for clarity: with Golgi in orange, COPI buds and vesicles in light purple, ERGIC in dark purple, ER in dark green and COPII vesicles in light green.

B. As in A, but no Golgi membranes are visible. The plasma membrane is depicted in azure.

Scale bar 100 nm

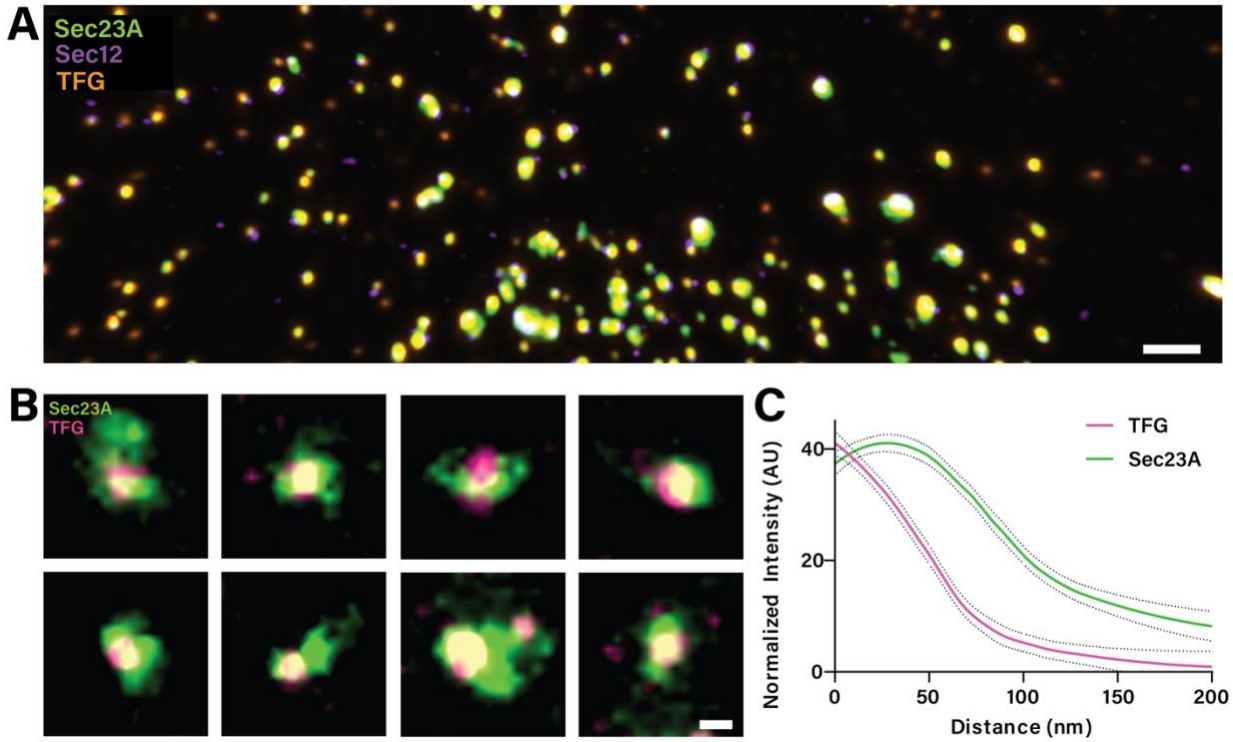

Figure 7

Co-localization of TFG and Sec23A in HaloTag-Sec23A RPE1 cells.

A. Three-color high resolution confocal fluorescence imaging of endogenous HaloTag-Sec23A dyed with HaloTag JFX650 ligand (green) and immunostained Sec12 (purple) and TFG (orange).

B. Two-color super resolution STED imaging of endogenous HaloTag-Sec23A dyed with HaloTag JFX650 ligand (green) and immunostained TFG (pink).

C. Averaged linescans of TFG (pink) and HaloTag-Sec23A (green) fitted from 50 measurements across 9 cells over 3 experimental repeats, showing the distribution of HaloTag-Sec23A signal from the center of TFG condensates extracted from the two-color super resolution STED imaging. Standard error is shown with by the dotted lines.

Scale bars overviews: 1 µm, insets: 100 nm

classes of vesicles. Consequently, we sought to understand the spatial relationship between COPI, COPII and TFG. Since phase separated structures do not typically exhibit recognizable features in cryo-tomograms, we used super resolution STED imaging to gather additional information regarding TFG distribution at ERESs (Figure 7B). Based on these data, TFG condensates appeared to be surrounded by COPII-positive membranes (Figure 7C). This is consistent with TFG clustering COPII carriers, as opposed to restricting the entry of COPI.

Discussion

In this study, we used fluorescence and cryo-electron microscopy to visualize ERESs in situ in a human cell line expressing an endogenously tagged form of the COPII component Sec23A. We obtained cryo-tomograms with information extending to 1.5 nm resolution, where we were able to detect coated vesicles and define their molecular identity. We found that ERESs consist of COPII coated vesicles and buds emanating from the ER, next to vesicular-tubular membranes that are independent from the ER and from which COPI vesicles are budding. Using STED and other super resolution imaging techniques, we define these structures as ERGIC membranes.

In contrast to previous interpretations of lower-resolution fluorescence and volume EM data[5,31], we did not observe tunnels connecting the ER with either ERGIC or Golgi membranes, nor did we find any evidence of "coated collars". We were able to resolve several membrane tubules extending from the ER; however, they were not coated and always connected with another ER cisterna whenever we could trace their destinations, consistent with the well-established network-like nature of this organelle.

Our data do not exclude that COPII-derived tunnels exist in cells. As our workflow is biased towards clusters of vesicles, we will need a cryo-CLEM approach with more accurate targeting of fluorescent puncta, without having to rely on an intermediate low-magnification tomogram step. However, our results clearly and unambiguously show that the main mode of ER exit – at least in unperturbed human epithelial cells – relies on COPII and COPI coated vesicles (Supplementary Figure 6). Our results support our current understanding of how coats can remodel membranes and generate curvature. The alternative scenario, where a protein collar would serve as gatekeeper without forming a coat, lacks both experimental support and a physical mechanism for curvature generation.

Live cell fluorescence imaging studies have shown COPI-labeled structures moving from peripheral ERESs to the Golgi at speeds compatible with microtubule motor-dependent movement, and it has been proposed that COPI might serve as an anterograde coat from the ERGIC to the Golgi[5]. We failed to see any association between COPI coated vesicles or buds and microtubules, and no such interaction has been reported to date. It is therefore unlikely that independent small COPI coated vesicles traverse the cytosol across tens of microns to be delivered to the Golgi. We believe our results are more compatible with a scenario where ERGIC clusters move en bloc towards the Golgi in a microtubule motor-dependent manner, while COPI

dynamically associates with the moving ERGIC to retrieve and recycle cargo receptors and escaped ER-resident proteins back to nearby ER.

The molecular underpinning of how and when the ERGIC is transported remains to be resolved. While we did see microtubules in >70% of our tomograms, these did not appear to be associated with ERGIC membranes, and their numbers were similar to those seen in non-ERES containing tomograms. Therefore, we hypothesize that ERGIC membranes might engage with microtubules at a temporally delayed point, after dissolution of the source ERES. However, there is evidence that ERESs are long lived[44], so an alternative hypothesis is that anterograde ERGIC membranes may diffuse away from their source ERES and engage with microtubules at a spatially separated site. More work including live fluorescence and cryo-ET is needed to establish the relative lifetime and movement of ERES and ERGIC membranes and their cytoskeleton engagement.

Both COPI and COPII coated vesicles have density features consistent with in vitro reconstituted coated vesicles, validating previous structural efforts to characterize their molecular architecture. Coated vesicles and buds display a variety of shapes and sizes (Figure 2, Figure 3, Figure 5 and Supplementary Figure 5), consistent with flexible assembly mechanisms that provide a suitable platform for regulation. COPII coated membranes clearly show the inner and outer coat profiles described in vitro[11,12] (Figure 2). While our in situ data were not conducive to structure determination, the variability in size and shape of COPII coated carriers strongly suggests that the mode of assembly characterized in vitro, with locally ordered inner coat patches stabilized by outer cages of variable geometries[12], is plausible.

Fitting ellipsoids and spheres into coated vesicles revealed that COPI vesicles are on average smaller and more variable in size and shape than COPII (Figure 5E), potentially suggesting greater flexibility in the geometry of the COPI coat or less stringent regulation of vesicle scission.

When we compared the number of coated buds and free coated vesicles, we found that COPII and COPI display opposite behavior (Figure 5D). COPI is found more often around buds, indicative of either faster uncoating or slower curvature acquisition and delayed scission. It has been shown that GTP hydrolysis on Arf1 is triggered in stages by Arf-GAPs that are bound to different subunits of coatomer. It was proposed that the second wave of GTP hydrolysis, leading to uncoating, might happen once the COPI subunits are arranged around high membrane curvature (i.e. a complete vesicle)[16,22]. This would explain why we see few coated free vesicles, as uncoating would happen fast after vesicle completion.

In the case of COPII, the coat seems more persistent on free vesicles (Figure 5E). It remains unclear when uncoating happens for COPII, but it has been shown that even upon GTP hydrolysis of Sar1, the inner coat components remain attached to vesicles for some time[45], probably via interaction with cargo and through maintenance of a stable outer cage. Full uncoating is likely to occur once the outer coat cage detaches from the inner coat, weakening its lattice arrangement. TFG has previously been implicated as an uncoating factor that acts by competing with Sec31 for Sec23 binding and is a likely candidate for triggering full uncoating[39,46]. Our STED data suggests that

TFG clusters neighboring vesicles, consistent with a model where fully coated vesicles encounter TFG condensates where they are stripped down[39,46]. We see no evidence supporting the proposed model for TFG to form sieve-like structures separating areas of COPII- and COPI-mediated transport[43].

This work provides a framework to advance the ongoing discourse around the molecular nature of ER-derived transport carriers, but it is by no means exhaustive. COPII is required for ER exit of a variety of cargo in all cell types, and our results leave the open question of how ERESs are uniquely organized in various specialized cell types.

Highly secretory cells tend to have significantly increased expression levels of secretory pathway components, including COPII. It is often the case that a particular paralogue of COPII is upregulated in such cells, for example Sar1B over Sar1A in plasma cells or early spermatids, or Sec24D in many secretory cells including plasmablasts and hepatocytes (https://www.proteinatlas.org/). It remains to be answered whether different paralogues influence the organization of ERESs and the morphology of carriers.

The organization of the early secretory pathway in neurons will also need to be investigated. Although the majority of COPII-mediated transport has been suggested to take place in the cell body, ERES components are found in both axons and dendrites, potentially contributing to local expression of membrane proteins, including signaling receptors and cell adhesion factors[47]. Depletion of Sar1 has been shown to inhibit axon outgrowth, as does overexpression of a dominant negative isoform of Sar1[48]. Additional cryo-ET studies are necessary to determine the structure and organization of neuronal ERESs.

It is also hard to reconcile what we observe in epithelial cells with ER exit of large cargo, which are physically incapable of being packaged into 60-90 nm transport intermediates and yet show dependence on COPII. Collagen secretion has long intrigued researchers as procollagens constitute one of the most abundant classes of secretory cargo, yet their size (up to 500 nm) is prohibitively large for incorporation into canonical vesicles. Several models for collagen ER exit have been proposed, from large-coated carriers to tubules and tunnels[32,33,49–54]. A number of factors that contribute to COPII-mediated transport are necessary for collagen secretion, and certain mutations in COPII only affect collagens, leading to disease[55–61]. It is therefore possible that COPII transport has adapted and evolved in collagen secreting cells. We speculate that regulation of 'normal' COPII functions could lead to the generation of procollagen competent carriers. For example, tuning of coat assembly and disassembly rates could be sufficient in producing larger or tubular carriers, and a delay in scission could lead to the generation of 'tunnels' connecting ER and ERGIC without re-inventing COPII molecular mechanisms. Factors from the Tango1 family are likely to be involved in this regulation[52,56]. The only way to answer this mystery is to directly visualize collagen carriers at a resolution sufficient to discern coated membranes.

Materials and Methods:

Cell culture

Wild type human retinal pigmented epithelial cells (RPE-1) were obtained from ATCC and were cultured in DMEM/F12 (ThermoFisher Scientific) plus 10% FBS, L-glutamine and 1% Pen/Strep (Bio Basic). CRISPR modified Halo-Sec23A and SNAP-tag-ERGIC-53 RPE-1 cells were sourced as described in[34] an maintained in analogous conditions to wild type.

Fluorescence microscopy

For immunofluorescence studies, cells were labeled with JFX650-HaloTag ligand (generously provided by Luke Lavis) and subsequently fixed using 4% paraformaldehyde at 37°C for 8 minutes or 100% methanol at -20°C for 10 minutes, followed by permeabilization and antibody labeling (1 mg/ml) at 4°C overnight. Immunofluorescence studies were conducted using validated antibodies directed against Sec16A (Bethyl Laboratories; A300-648A), Sec31A (BD Sciences; 612351), TFG (Novus Biologicals; NBP2-62212), ERGIC-53 (Santa Cruz Biotechnology; sc-66880), and COPB (Santa Cruz Biotechnology; sc-393615). After thorough washing, coverslips were incubated with secondary antibodies (AlexaFluor conjugates) for 1 hour at room temperature in the dark and mounted using Prolong Diamond Antifade. Slides were cured for 24 hours in the dark at room temperature before imaging.

Confocal imaging studies were conducted using a Nikon Ti2 spinning disk confocal microscope equipped with a 60x oil immersion objective (1.4 NA) and a Hamamatsu ORCA-Flash4.0 sCMOS camera. Imaging datasets were comprised of 25-35 sections separated by 0.3 µm (depending on sample thickness).

3-color high-resolution confocal imaging was conducted on a Nikon AX R imaging system with NSPARC using a 100x SR HP Apo TIRF oil immersion objective (1.49 NA). Data were further processed by Nikon proprietary 'denoise' software settings to elucidate their geometry. Imaging datasets were comprised of 32-43 sections separated by 0.08 µm. The TetraSpeck Fluorescent Microspheres Size Kit (ThermoFischer) was imaged to establish the field of view without chromatic aberration, as determined by complete overlap of fluorescent beads in all channels. The center third of the field of view was identified as devoid of chromatic aberration and thus used for analysis.

For STED microscopy, cells were labeled with JFX650-HaloTag Ligand and fixed as described above. Alexa Fluor 594 secondary conjugates were used prior to mounting using Prolong Diamond Antifade. Coverslips were cured at room temperature in the dark for 24 hours prior to imaging on an Abberior STEDYCON super-resolution imaging system using the 775 nm depletion laser and a 100X Plan Apo Lambda objective (1.45 NA).

Confocal and STED Image Analysis

To identify structures, the Spots Creation Wizard was used in Imaris Microscopy Image Analysis Software (Oxford Instruments). The software subtracts background and identifies spots based on the intensity at the center of each spot. Quality thresholds were established per channel per experiment to eliminate background staining.

To quantify the number of ERESs per cell, the total number of Sec31 positive punctate structures was counted in control RPE-1 cells (n = 32 cells, N = 2).

To quantify distance between markers in images acquired on the Nikon AXR system, distance thresholds were set to eliminate non-co-located structures. The threshold for HaloTag-Sec23A and Sec16A was 0.175 µm and HaloTag-Sec23A and β-COP was 0.2 µm. Various thresholds were tested to ensure data integrity. The distance between the center intensities of co-located structures was quantified using the Shortest Distance tool in Imaris. For each condition at least 1900 distances were measured from at least 10 cells across 2 experimental repeats.

To quantify the percentage colocalization between COPI and COPII, a distance threshold of 0.2 µm was used and the number of co-localized spots was divided by the total spots counted in the analysed field of view of 21 images across four experimental repeats.

To create the linescans, Imaris was used to pick spots at the intended beginning and end of the line of interest. The intensity profile of this line was exported and data from at least 30 structures were used to calculate the averaged linescan via 2 degree local polynomial regression, performed using the loess function from the stats package in R. For TFG and HaloTag-Sec23A, the line originated at the highest intensity center of the TFG structure and passed through the entirety of the neighboring HaloTag-Sec23A structure. For HaloTag-Sec23A and Sec16A, the individual linescans were generated by measuring the fluorescence originating adjacent to the Sec16A puncta and passing through the entirety of both the Sec16A and neighboring Sec23A puncta. The intensity values were normalized for display purposes.

EM

Grid preparation

Quantifoil R 2/2, Mo 200 mesh grids with Holey Carbon Films (Quantifoil Micro Tools GmbH) and UltrAuFoil R 2/2, Au 200 mesh grids with Holey Gold Supports (Quantifoil Micro Tools GmbH) were both used in this work. Grids were secured in a 6-well plate using the Linkam cartridge and cartridge holder system, all of which were plasma cleaned using the Tergeo-EM (PIE scientific) and irradiated with UV light for 1 hour at room temperature to sterilize. Next, the grids, cartridge and cartridge holder were incubated with media for 30 mins.

RPE-1 cells expressing HaloTag-Sec23A from its endogenous locus were plated onto grids at a density of 2.5×10^5 cells/mL and topped up with media to ensure the cartridge system was fully

submerged. Cells were cultured on grids for ~ 24 hours (37°C with 5% CO_2). Cell confluency and distribution was visually inspected using a phase contrast optical microscope before staining with 1 μL/mL Oregon Green-HaloTag Ligand (Promega) following manufacturer instructions. Cells were then moved to a 37°C incubator close to the plunge freezer. Each cartridge, containing a maximum of 3 grids, was moved into an individual cartridge holder and tissue culture dish, allowing batches of 3 grids to be processed for plunge freezing, minimizing the time each grid spends outside the incubator.

Grids were manually back blotted to remove media. 4 μL of 0.5 mg/mL Dynabeads MyOne Carboxylic Acid (ThermoFisher Scientific) resuspended and diluted in 10% glycerol, were added to the cell coated grid face and incubated, horizontally for ~ 30 s at room temperature before transfer to the LeicaGP (Leica) chamber (37°C and 70% humidity). If the droplet was lost during transfer, it was readded in situ. Grids were then back-blotted for 8 s before plunge freezing in liquid ethane and stored in liquid nitrogen.

Cryo-grids were clipped into autogrids (Thermo Fisher Scientific) and screened for their ice thickness and cell distribution on a 200kV Glacios or Talos electron microscope (Thermo Fisher Scientific) prior to milling.

Cryo-FIB Lamella preparation

Lamellae were prepared on an Aquilos 2, a dual beam FIB/SEM equipped with an iFLM correlative system (Thermo Fisher Scientific) and long-operation liquid nitrogen dewar with 175 L capacity (SubAngstrom). First, SEM tile-sets were collected and aligned to the previously acquired TEM atlases in MAPS v3.30 (Thermo Fisher Scientific). Potential areas for milling were identified based on suitable ice-thickness and their location within the grid square.

Next, fluorescence Z-stacks (0.1 μm steps) were acquired at these sites using the integrated iFLM module - 20x objective (Zeiss Epiplan-Apochromat, NA 0.7, Piezo-driven), filter cube (Semrock LED-DA/FI/TR/Cy5-B-000, Quadband), camera (Basler ace 2, 2A4504-5gmPRO; Sony IMX541 CMOS sensor) and LED source (CoolLED, 365 nm/450 nm/550 nm/635 nm). The reflection, 470 nm and 565 nm channels were acquired at 0.5%, 10% and 10% laser power and 1.5 ms, 200 ms and 200 ms exposure time respectively. The 565 nm channel was acquired to aid discrimination between fluorescence from Oregon Green-HaloTag-Sec23A, auto-fluorescence and fluorescent fiducials.

The fluorescence and reflection Z-stacks were imported into MAPS and aligned to the SEM tile-set using three reference points. Clusters of Oregon Green-HaloTag-Sec23A signal were preferentially chosen as sites of interest to increase the likelihood of milling through COPII-rich regions in the cell. Precise targeting of the site of interest was further aided by selection of a corresponding fluorescent Dynabead fiducial found in the same channel.

Post fluorescence imaging, grids were sputter coated with inorganic platinum (Platinum Black) for 15 seconds at 30 mA, then coated with organometallic platinum

(Trimethyl(methylcyclopentadienyl)platinum(IV)) using the gas injection system (GIS) for 45 seconds, followed by another sputter coat for 15 seconds at 30 mA to further enhance sample conductivity.

Lamella positions, eucentric height and milling angles were automatically calculated in AutoTEM 2.4 (Thermo Fisher). Final lamella placement was guided by the site of interest/fiducial pair that was added in MAPS and identified in the FIB image. The length and position of the lamella was optimized for each cell. Lamellae were produced using a Gallium beam, operating at 30 kV, in a stepwise manner starting at a beam current of 1.0 nA for rough milling and decreasing to 0.5 nA and 0.3 nA for medium and fine milling. Thinning was then performed in two stages with a beam current of first 50 pA, and then 30 pA. Target milling angles ranged from 9° to 15° and the target lamella thickness was set between 150 and 250 nm.

Following thinning, 0.2 µm step Z stacks were acquired as described above, adjusting the 470 nm exposure time as required to visualise on-lamella signal and determine the targeting success of the milling. Prior to unloading a second sputter coat at 7 mA for 15 seconds was applied to reduce beam-induced specimen movement of the lamella in the TEM. Grids were unloaded and then immediately loaded into a Titan Krios G2 TEM microscope (Thermofisher) to limit lamella breakage and reduce ice contamination during storage.

Cryo-electron tomography data collection

Medium-magnification montages were collected from intact lamella (3 nm pixel size with 100 um defocus) in a Krios G2 TEM running Tomography v5.19. The montages were imported into MAPS software (Thermo Fisher Scientific) where they were manually aligned with fluorescence Z-stacks collected from thinned lamellae to assist with identification of regions of interest for tilt series collection.

Lower-magnification tilt series (Supplementary Table 1) with a restricted tilt range and lower dose were collected from areas on the lamella that retained Oregon Green-HaloTag-Sec23A signal. The resulting tomograms were inspected for potential COPII-containing ERESs and served as guide for a second tilt series collected at higher magnification with a higher total electron dose (Supplementary Table 1).

Parameters	**Low magnification cryoET**	**High magnification cryoET**
Microscope	Titan Krios G2	Titan Krios G2
Voltage (kV)	300	300
Camera	Gatan K2	Gatan K2
Energy filter	Bioquantum	Bioquantum
Slit width (eV)	20	20
Magnification	19500	64000

Pixel size (Å/px)	7.3	2.25
Dose per tilt image	0.68	3.5
Total electron dose (e/Å)	8.8	148
Targeted defocus range (µm)	-50	"-7 to -10"
Tilt range	"-30° to +30°"	"-69° to +54°"
Tilt increment	5°	3°
Automation software	Tomography 5.19	Tomography 5.19

Tomogram Processing

Tilt series alignment and reconstruction

The low magnification, low dose, restricted tilt-series were reconstructed using IMOD's motion correction (alignframes)[62] and AreTomo v.1.3.4[63] for alignment and reconstruction, allowing quick access to reconstructed tomograms for visual inspection with minimal manual input. The resulting 138 tomograms were binned to a final pixel size of 14.6 Å and were inspected using IMOD. 94 tomograms were identified as containing regions indicative of ERESs and were used to direct high magnification tilt series acquisition.

High-magnification tomograms were initially reconstructed as described above and IMOD was used to inspect and identify tomograms containing regions of interest. 63 tilt series containing regions of interest were reprocessed following the WarpTools pipeline, including motion correction, CTF and defocus handedness estimation (https://warpem.github.io/warp/). Tilt series were aligned using the WarpTools etomo patch tracking wrapper[62]. Bad tilts were manually removed, and poorly aligned tilt series were manually improved with etomo. CTF-corrected tomograms were reconstructed at a pixel size of 10 Å and used to pick ribosomes for further improvement of alignments with Warp/M[35].

PyTOM_TM[64] was used to identify ribosomes in reconstructed tomograms, using a human ribosome map (EMD-36178) as a template (Supplementary Figure 3). Per-tomogram thresholds to select the highest cross-correlation peaks were automatically determined. Most peaks clearly overlapped with ribosomes (Supplementary Figure 3), and false positives were easily identified as these tended to cluster on dark features such as contamination. These were manually cleaned using the ChimeraX plugin ArtiaX[65], obtaining a total of 16543 ribosomes. The picked ribosomes were exported at a pixel size of 4 Å, averaged and low pass filtered to 150 Å to create a starting reference, which was used to refine the ribosome dataset using relion 3D Refine[66], achieving a resolution of ~20 Å. To test for reference bias and confirm tomogram handedness, we repeated the relion refinement step using a mirrored copy of the starting reference. This yielded a ribosome map which had reverted to the correct hand and was in a rotated orientation compared to the template used for picking (Supplementary Figure 3). Reassured that the ribosome structure we obtained was real, we further refined it using M, obtaining a map at ~15 Å resolution after 5 iterations. The resulting

alignments were used for a final round of tomogram reconstruction, yielding optimized CTF-corrected tomograms suitable for downstream analysis.

Tomogram analysis

Tomograms were denoised using the WarpTools denoiser prior to segmentation with membrain-seg v2[67]. Deepdewedge[68] was also used as an alternative denoiser for tomogram visualization and figure/movie creation. Membranes were further manually segmented using Segger[69] and individual coated membranes were initially labelled as COPI or COPII based on their visual appearance (Figure 2).

Segmented membranes from all coated vesicles (COPI and COPII together) were expanded by 15 pixels and used as masks for template matching against non-denoised, CTF corrected tomograms using PyTOM_TM. We used EMD-19417 as template to search for COPII, and EMD-3968 to search for COPI. All peaks were extracted and manually thresholded based on their cross-correlation value using ArtiaX. Template matching confirmed our manual assignments, with the COPII template giving the highest cross-correlation peaks predominantly around membranes which were originally labelled as COPII coated, and vice versa.

COP particle picking and alignment

Coordinates oversampling membrane surfaces from the 10 Å/pixel reconstruction were defined based on segmentations using in-house Matlab scripts. Points were separated by 50 Å and yaw and pitch angles were assigned based on particles having a normal orientation to the membrane. In plane-rotation was randomized. Local curvature was calculated based on the angle between each point and its neighbours, and points with local curvature defined by diameters smaller than 30 Å were removed (these were often found at the rims of segmented membanes). Particles from either COPII or COPI membranes were extracted in 64 voxel boxes and averaged using dynamo. Particles were aligned for 5 iterations against the starting average using dynamo, allowing for no angle refinements, and shifts of 2x2x6 pixels in x, y and z direction respectively, and applying a low pass filter of 12 pixels. A shell-shaped mask generously encompassing the membrane and the coat layers was used.

Morphology analysis

Segmented individual coated membranes were manually classified as vesicles or buds based on their corresponding tomogram density. The morphology of these structures was analyzed using scripts adapted from[38]. These scripts approximated the segmented membrane structure to a fitted sphere and ellipsoid. The best fitted ellipsoid and sphere for each structure was manually inspected using pyvista[70] to determine which fit best described the structure. The volume and sphericity of the best fitted shape was plotted using seaborn[71] and matplotlib[72].

Statistics

Statistical analyses were performed using the stats module of SciPy[73]. The difference between both volumes and sphericities were performed using the Mann-Whitney U test and the median values were quoted as the distributions were non normal. The differences between the distributions of these groups were performed using the Kolmogorov-Smirnov test.

The two-proportion Z-test was performed to assess the statistical significance of the number of filaments in ERES versus non-ERES tomograms.

Acknowledgements

We thank the Structural Biology Science Technology Platform at the Crick for technical and computational support. We thank Elizabeth Miller from the University of Dundee and Patrick Phillips from the Francis Crick Institute for feedback on the manuscript. This work was supported by grants to G.Z. from the European Research Council (ERC-StG-2019 grant 852915). Work in the group of A.A. was supported in part by a grant from the National Institutes of Health (GM134865).

Contributions

Conceptualization, G.Z.; funding acquisition, G.Z., A.A; fluorescence microscopy, J.F and A.A. sample preparation for cryo-EM, K.D. and S.V.D.V.; cryo-FIB/SEM and cryo-ET data collection, K.D. and A.N.; cryo-ET data processing, K.D. and G.Z.; writing (original draft), K.D. and G.Z.; writing (revisions), all authors.

Supplementary Figures

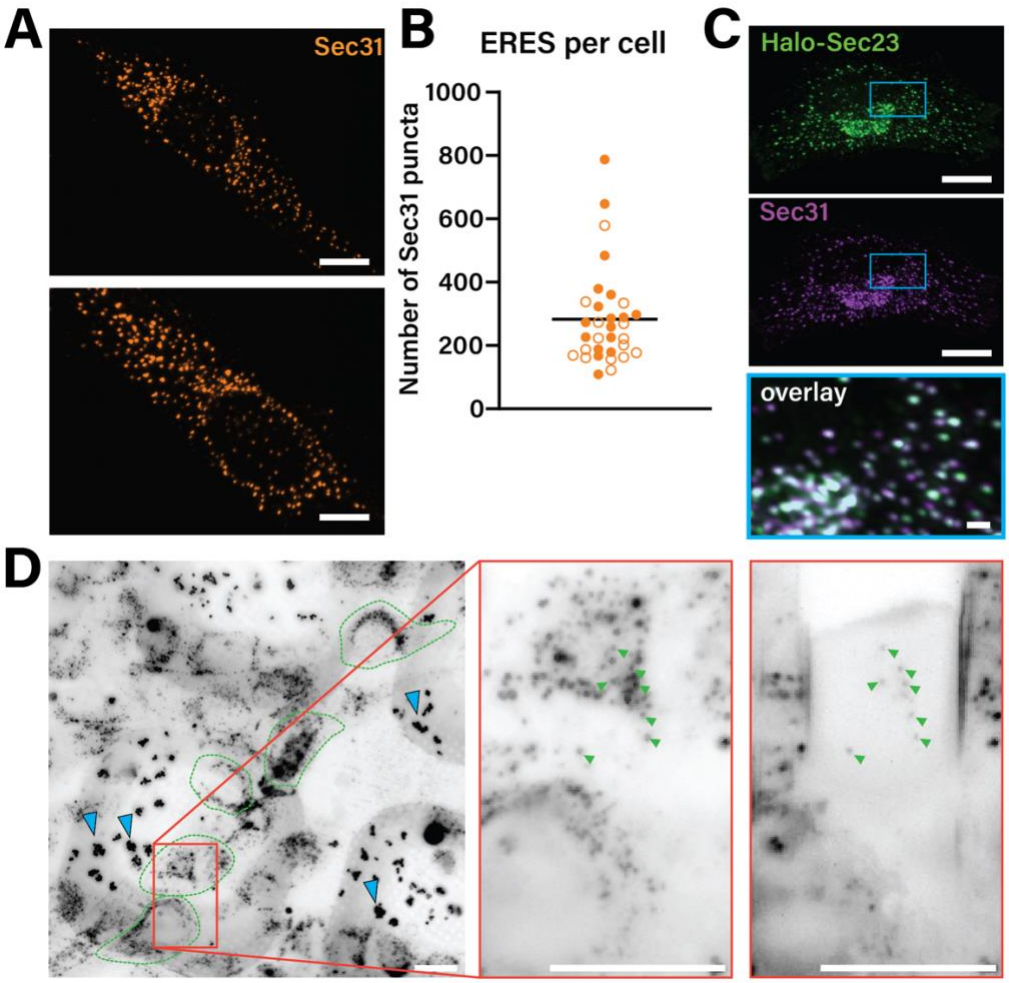

Supplementary Figure 1

HaloTag-Sec23A is a suitable candidate for investigating ERES structure.

A. *Wild type RPE1 cells immunostained against Sec31A.*
B. *Scatter plot of number of Sec31A positive structures in wild type RPE1 cells, colour coded by experimental repeat, n = 32 cells.*
C. *HaloTag-Sec23A-RPE1 cells dyed with JFX650-HaloTag ligand (green) and co-stained using an antibody directed against Sec31A (purple). Inset highlights tight colocalization of HaloTag-Sec23A fusion protein and endogenous Sec31A.*
D. *Example cryo-fluorescence wide field image of HaloTag-Sec23A-RPE1 cells grown on grids stained with Oregon Green HaloTag ligand before and after milling. HaloTag-Sec23A displays a punctate staining pattern throughout the cytoplasm and is concentrated at the perinuclear region. The red box in the left panel indicates the digitally magnified region in the other panels which show cryo-fluorescence before (middle panel) and after (right panel) milling. Four cells are indicated by green dotted outlines. Blue arrow heads indicate clusters of fluorescent fiducials. Green arrows indicate fluorescent puncta visible both before and after milling.*
   Scale bars: 10um, inset in panel C: 1um.

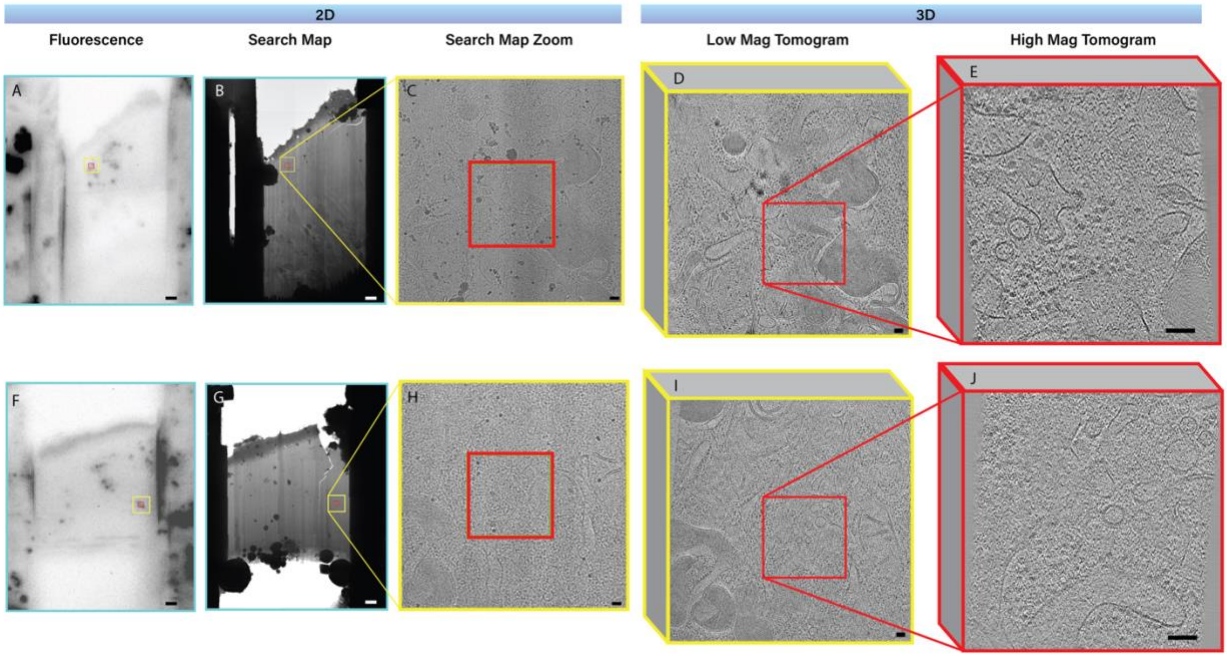

Supplementary Figure 2

Workflow for targeting ERESs on FIB/SEM lamellae.

A. Cryo-fluorescence maximum intensity projection from a FIB/SEM lamella of HaloTag-Sec23A RPE-1 cells stained with Oregon Green HaloTag ligand, acquired with the Aquilos 2 iFLM module. The yellow and red boxes highlight the areas subsequently imaged for low and high magnification tilt series acquisition.

B. The same lamella viewed in the TEM at low magnification (the search map).

C. A digitally zoomed version of B, showing the region encompassed by the yellow box in A. The presence of ERESs or more generally of membrane vesicles and tubules is not obvious.

D. Slice through the xy plane of a reconstructed cryo-tomogram acquired at low magnification around the region outlined by the yellow box.

E. Slice through the xy plane of a reconstructed cryo-tomogram acquired at high magnification around the region outlined by the red box.

F-J. Another example as in A-E.

Scale bars A,B,F,G: 1 um, C,D,E,H,I,J: 100 nm

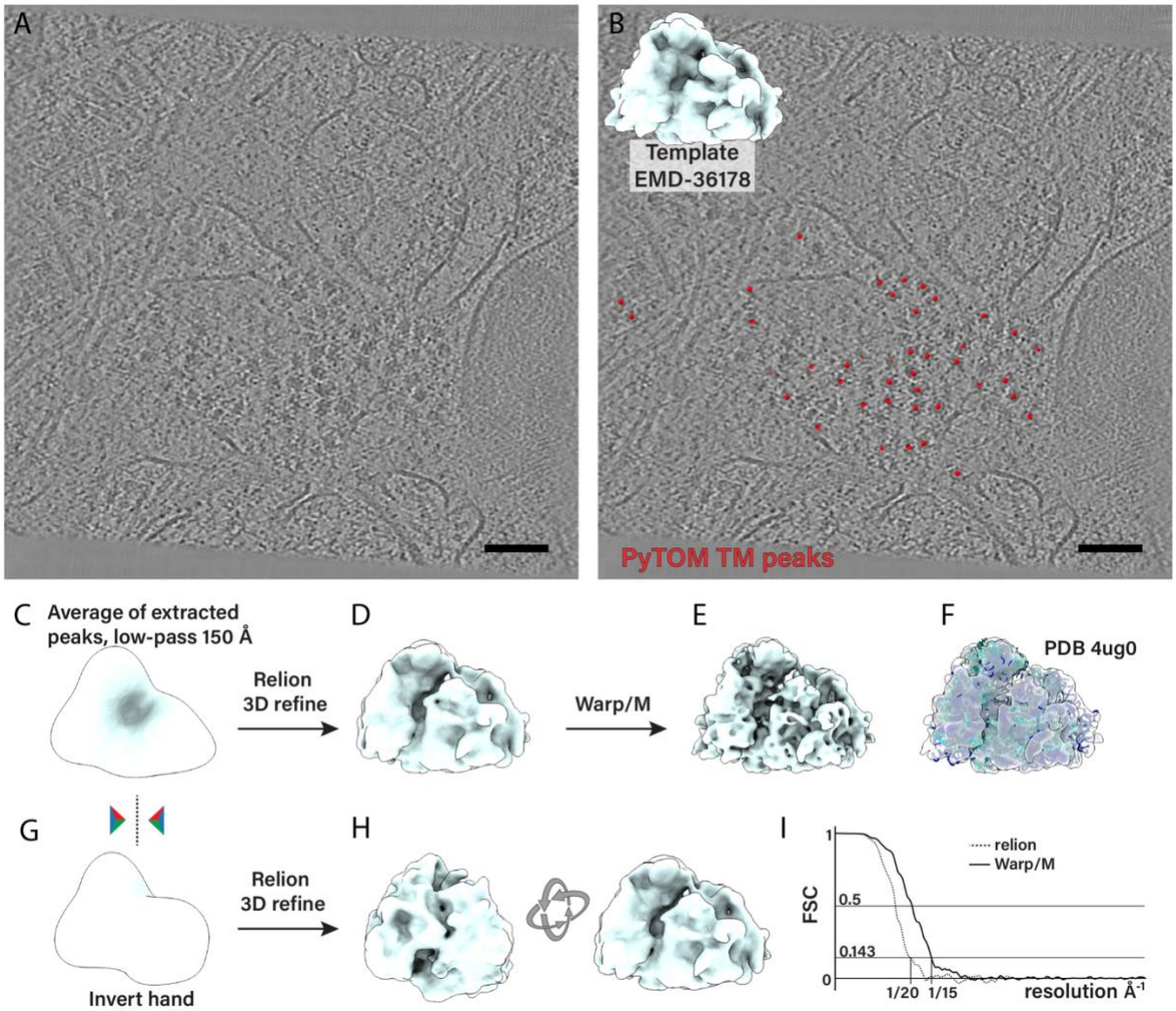

Supplementary Figure 3

Subtomogram averaging of ribosomes.

- *A. An xy slice through a reconstructed tomogram, where ribosome density is visible.*
- *B. As in A, with ribosome cross-correlation peaks from PyTOM_TM in red. Inset: reference used for template matching.*
- *C. Starting reference for alignments in relion, obtained by averaging PyTOM_TM peaks and low-pass filtering at 150 Å.*
- *D. The map obtained after one round of 3D refinement in relion4.*
- *E. The map obtained after 5 rounds of refinement in WARP/M.*
- *F. The map in E, with a fitted atomic model (PDB 4ug0).*
- *G. The map in C was mirrored to obtain a new staring reference for 3D refinements in relion*
- *H. The map obtained after one round of 3D refinement in relion against the mirrored starting reference, viewed in the same coordinate system (left) and rotated to match the view of the map in D.*
- *I. Gold standard Fourier Shell Correlation between half maps from the 3D refinement in relion (map in panel D, dotted curve), and WARP/M (map in panel E, solid curve). Resolutions at 0.143 threshold are 20 and 15 Å respectively.*

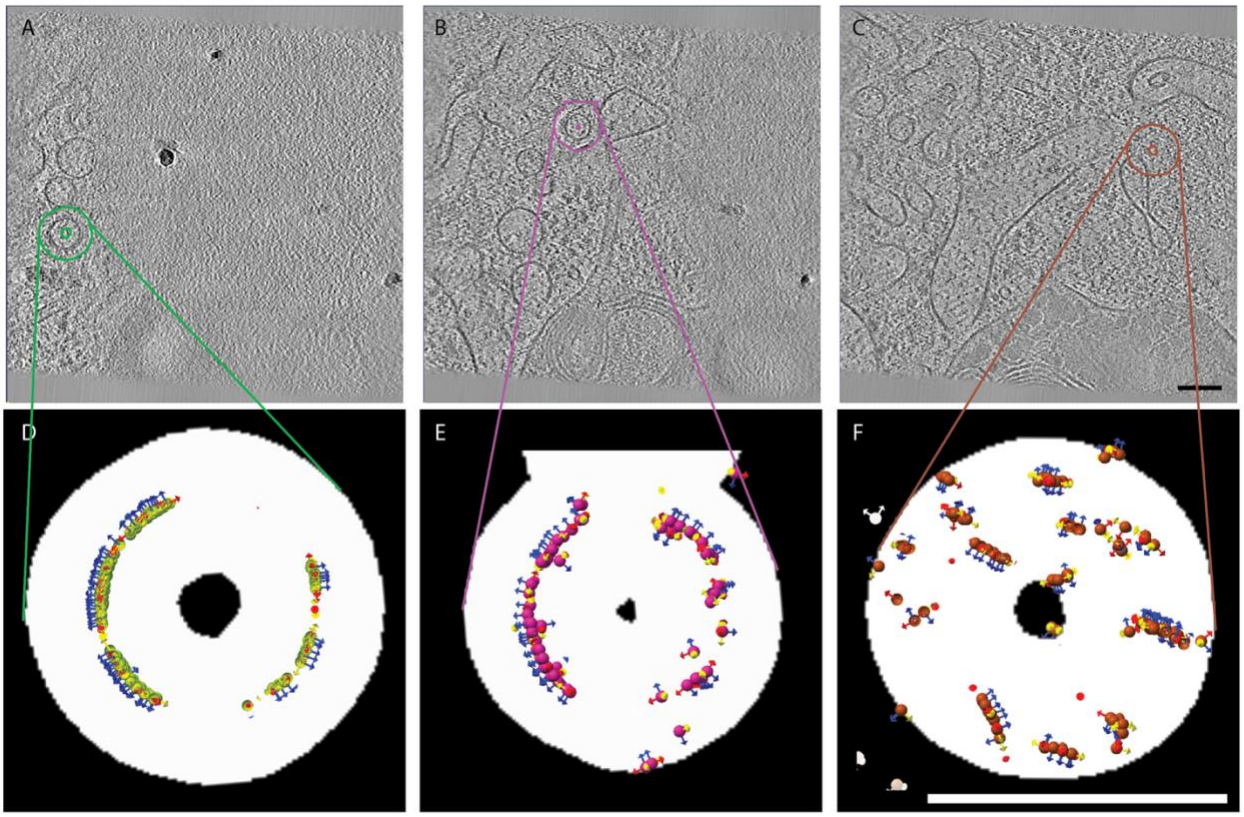

Supplementary Figure 4

COPI and COPII template matching.

A. *Slice through the xy plane of a tomogram overlayed with the outline of a mask used to run template matching. The mask at this plane is seen around a COPII coated vesicle.*
B. *Slice through the xy plane of a tomogram overlayed with the outline of a mask used to run template matching. The mask at this plane is seen around a COPI coated vesicle.*
C. *Slice through the xy plane of a tomogram overlayed with the outline of a mask used to run template matching. The mask at this plane was randomly applied as control.*
D. *A map of in vitro assembled COPII inner coat (EMD-19417) was used as template to search cryo-tomograms that were loosely masked around all coated membranes. Highest cross-correlation peaks are mapped onto the tomogram using ArtiaX, and a representative COPII-coated vesicles is shown. Peak positions are shown in green, and their orientations by blue, yellow and red arrows. The mask profile is in white against a black background.*
E. *A map of in vitro assembled COPI coat (EMD-3968) was used as template to search cryo-tomograms that were loosely masked around all coated membranes. Highest cross-correlation peaks are mapped onto the tomogram using ArtiaX, and a representative COPI-coated vesicles is shown. Peak positions are shown in purple, and their orientations by blue, yellow and red arrows.*
F. *A map of in vitro assembled COPI coat (EMD-3968) was used as template to search cryo-tomograms that were loosely masked at random places (a mask was applied to the wrong tomogram). Highest cross-correlation peaks are mapped onto the tomogram using ArtiaX, and a representative COPI-coated vesicles is shown. Peak positions are shown in brown, and their orientations by blue, yellow and red arrows.*

Scale bars: 100 nm

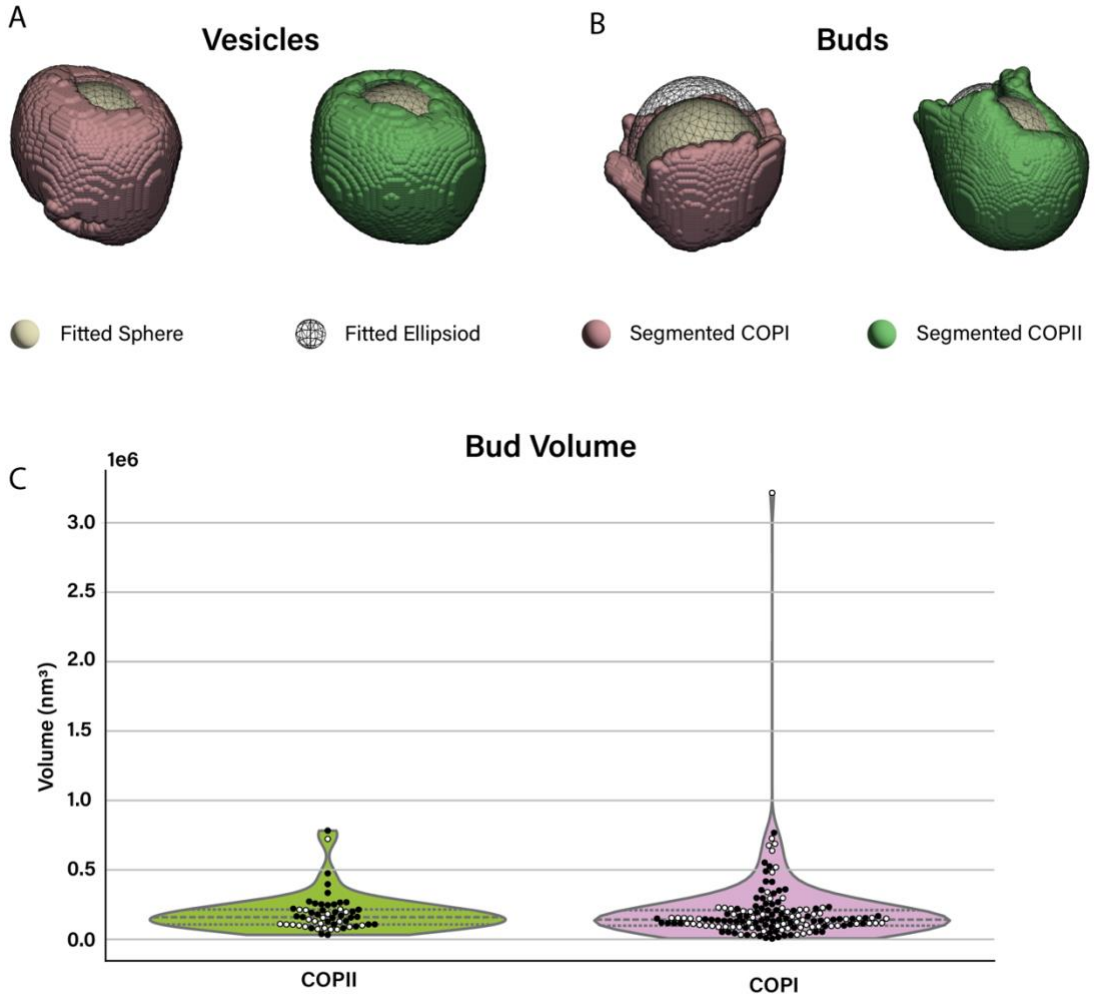

Supplementary Figure 5

Morphometric analysis of coated vesicles and buds.

A. Examples of fitted spheres and ellipsoids for segmented COPI and COPII vesicles.
B. Examples of fitted spheres and ellipsoids for segmented COPI and COPII buds.
C. Violin plot of the estimated volume of COPI and COPII coated buds. White and black circles indicate buds best fitted by a sphere and ellipsoid respectively. Grey dashed and dotted lines represent the median and interquartile range respectively.

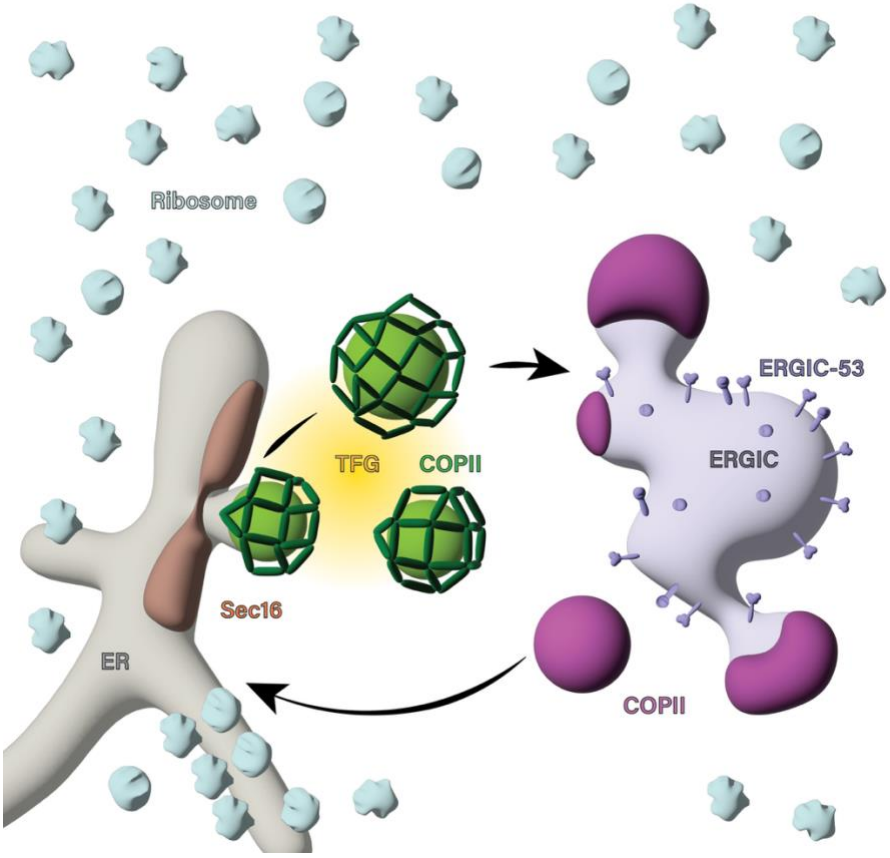

Supplementary Figure 6

An updated model of the mammalian ERES. COPII coated vesicles bud off Sec16A-positive segments of the ER membrane in ribosome-free regions of the cytosol. COPII vesicles are clustered by TFG in the area between the transitional ER and the ERGIC. COPI vesicles bud off ERGIC vesicular-tubular membranes and are found in close proximity to COPII.

Movie 1

A video showing a representative tomogram. Z slices through the xy pane of the tomograms are shown, followed by overlay with the membrane segmentation. Cross correlation peaks for COPII and COPI template matching are shown as green and purple dots respectively, followed by coloring the segmented membranes in the corresponding color.

References

1. Downes, K. W. & Zanetti, G. Mechanisms of COPII coat assembly and cargo recognition in the secretory pathway. *Nat Rev Mol Cell Biol* (2025) doi:10.1038/s41580-025-00839-y.
2. Zanetti, G., Pahuja, K. B., Studer, S., Shim, S. & Schekman, R. COPII and the regulation of protein sorting in mammals. *Nature Cell Biology* **14**, 20–28 (2012).
3. Kurokawa, K. & Nakano, A. The ER exit sites are specialized ER zones for the transport of cargo proteins from the ER to the Golgi apparatus. *J. Biochem.* (2018) doi:10.1093/jb/mvy080.
4. Bannykh, S. I., Rowe, T. & Balch, W. E. The organization of endoplasmic reticulum export complexes. *Journal of Cell Biology* **135**, 19–35 (1996).
5. Weigel, A. V. *et al.* ER-to-Golgi protein delivery through an interwoven, tubular network extending from ER. *Cell* **184**, 2412-2429.e16 (2021).
6. Westrate, L. M., Hoyer, M. J., Nash, M. J. & Voeltz, G. K. Vesicular and uncoated Rab1-dependent cargo carriers facilitate ER to Golgi transport. *J Cell Sci* **133**, jcs239814 (2020).
7. Jamieson, J. D. & Palade, G. E. INTRACELLULAR TRANSPORT OF SECRETORY PROTEINS IN THE PANCREATIC EXOCRINE CELL : III. Dissociation of Intracellular Transport from Protein Synthesis. *Journal of Cell Biology* **39**, 580–588 (1968).
8. Barlowe, C. *et al.* COPII: a membrane coat formed by Sec proteins that drive vesicle budding from the endoplasmic reticulum. *Cell* **77**, 895–907 (1994).
9. Matsuoka, K. *et al.* COPII-coated vesicle formation reconstituted with purified coat proteins and chemically defined liposomes. *Cell* **93**, 263–275 (1998).
10. Novick, P., Ferro, S. & Schekman, R. Order of events in the yeast secretory pathway. *Cell* **25**, 461–469 (1981).
11. Hutchings, J. *et al.* Structure of the complete, membrane-assembled COPII coat reveals a complex interaction network. *Nature Communications* **12**, 2034 (2021).

12. Pyle, E., Miller, E. A. & Zanetti, G. Cryo-electron tomography reveals how COPII assembles on cargo-containing membranes. *Nat Struct Mol Biol* (2024) doi:10.1038/s41594-024-01413-4.

13. Stagg, S. M. *et al.* Structural basis for cargo regulation of COPII coat assembly. *Cell* **134**, 474–484 (2008).

14. Miller, E., Antonny, B., Hamamoto, S. & Schekman, R. Cargo selection into COPII vesicles is driven by the Sec24p subunit. *The EMBO Journal* **21**, 6105–6113 (2002).

15. Kuehn, M. J., Herrmann, J. M. & Schekman, R. COPII-cargo interactions direct protein sorting into ER-derived transport vesicles. *Nature* **391**, 187–190 (1998).

16. Arakel, E. C. & Schwappach, B. Formation of COPI-coated vesicles at a glance. *J Cell Sci* **131**, jcs209890 (2018).

17. Orci, L. *et al.* Budding from Golgi membranes requires the coatomer complex of non-clathrin coat proteins. *Nature* **362**, 648–652 (1993).

18. Aridor, M., Bannykh, S. I., Rowe, T. & Balch, W. E. Sequential coupling between COPII and COPI vesicle coats in endoplasmic reticulum to Golgi transport. *J Cell Biol* **131**, 875–893 (1995).

19. Stephens, D. J., Lin-Marq, N., Pagano, A., Pepperkok, R. & Paccaud, J. P. COPI-coated ER-to-Golgi transport complexes segregate from COPII in close proximity to ER exit sites. *J Cell Sci* **113 (Pt 12)**, 2177–2185 (2000).

20. Rowe, T. *et al.* COPII vesicles derived from mammalian endoplasmic reticulum microsomes recruit COPI. *J Cell Biol* **135**, 895–911 (1996).

21. Zanetti, G. *et al.* The structure of the COPII transport-vesicle coat assembled on membranes. *Elife* **2**, e00951 (2013).

22. Dodonova, S. O. *et al.* 9Å structure of the COPI coat reveals that the Arf1 GTPase occupies two contrasting molecular environments. *Elife* **6**, (2017).

23. Faini, M. *et al.* The structures of COPI-coated vesicles reveal alternate coatomer conformations and interactions. *Science* **336**, 1451–1454 (2012).

24. Barlowe, C. & Schekman, R. SEC12 encodes a guanine-nucleotide-exchange factor essential for transport vesicle budding from the ER. *Nature* **365**, 347–349 (1993).

25. Bi, X., Mancias, J. D. & Goldberg, J. Insights into COPII coat nucleation from the structure of Sec23.Sar1 complexed with the active fragment of Sec31. *Dev. Cell* **13**, 635–645 (2007).

26. Lord, C. *et al.* Sequential interactions with Sec23 control the direction of vesicle traffic. *Nature* **473**, 181–186 (2011).

27. Yoshihisa, T., Barlowe, C. & Schekman, R. Requirement for a GTPase-activating protein in vesicle budding from the endoplasmic reticulum. *Science* **259**, 1466–1468 (1993).

28. Donaldson, J. G., Cassel, D., Kahn, R. A. & Klausner, R. D. ADP-ribosylation factor, a small GTP-binding protein, is required for binding of the coatomer protein beta-COP to Golgi membranes. *Proc Natl Acad Sci U S A* **89**, 6408–6412 (1992).

29. Hara-Kuge, S. *et al.* En bloc incorporation of coatomer subunits during the assembly of COP-coated vesicles. *Journal of Cell Biology* **124**, 883–892 (1994).

30. Bykov, Y. S. *et al.* The structure of the COPI coat determined within the cell. *eLife* https://elifesciences.org/articles/32493 (2017) doi:10.7554/eLife.32493.

31. Shomron, O. *et al.* COPII collar defines the boundary between ER and ER exit site and does not coat cargo containers. *J Cell Biol* **220**, e201907224 (2021).

32. Raote, I. & Malhotra, V. Tunnels for Protein Export from the Endoplasmic Reticulum. *Annual Review of Biochemistry* **90**, 605–630 (2021).

33. Bunel, L., Pincet, L., Malhotra, V., Raote, I. & Pincet, F. A model for collagen secretion by intercompartmental continuities. *Proceedings of the National Academy of Sciences* **121**, e2310404120 (2024).

34. Kasberg, W. *et al.* The Sar1 GTPase is dispensable for COPII-dependent cargo export from the ER. *Cell Rep* **42**, 112635 (2023).

35. Tegunov, D., Xue, L., Dienemann, C., Cramer, P. & Mahamid, J. Multi-particle cryo-EM refinement with M visualizes ribosome-antibiotic complex at 3.5 Å in cells. *Nat Methods* **18**, 186–193 (2021).

36. Hutchings, J., Stancheva, V., Miller, E. A. & Zanetti, G. Subtomogram averaging of COPII assemblies reveals how coat organization dictates membrane shape. *Nature Communications* **9**, 4154 (2018).

37. Klumperman, J. *et al.* The recycling pathway of protein ERGIC-53 and dynamics of the ER-Golgi intermediate compartment. *J Cell Sci* **111 (Pt 22)**, 3411–3425 (1998).

38. Bieber, A. *et al.* In situ structural analysis reveals membrane shape transitions during autophagosome formation. *Proceedings of the National Academy of Sciences* **119**, e2209823119 (2022).

39. Hanna, M. G. *et al.* TFG facilitates outer coat disassembly on COPII transport carriers to promote tethering and fusion with ER-Golgi intermediate compartments. *Proc. Natl. Acad. Sci. U.S.A.* **114**, E7707–E7716 (2017).

40. Johnson, A. *et al.* TFG clusters COPII-coated transport carriers and promotes early secretory pathway organization. *EMBO J* **34**, 811–827 (2015).

41. Kasberg, W. *et al.* TFG regulates inner COPII coat recruitment to facilitate anterograde secretory protein transport. *MBoC* **35**, ar113 (2024).

42. McCaughey, J. *et al.* TFG Promotes Organization of Transitional ER and Efficient Collagen Secretion. *Cell Rep* **15**, 1648–1659 (2016).

43. Bogus, S. M. *et al.* A hollow TFG condensate spatially compartmentalizes the early secretory pathway. *Nat Commun* **16**, 3715 (2025).

44. Hammond, A. T. & Glick, B. S. Dynamics of transitional endoplasmic reticulum sites in vertebrate cells. *Mol Biol Cell* **11**, 3013–3030 (2000).

45. Sato, K. & Nakano, A. Dissection of COPII subunit-cargo assembly and disassembly kinetics during Sar1p-GTP hydrolysis. *Nature Structural & Molecular Biology* **12**, 167–174 (2005).

46. Hanna, M. G., Peotter, J. L., Frankel, E. B. & Audhya, A. Membrane Transport at an Organelle Interface in the Early Secretory Pathway: Take Your Coat Off and Stay a While. *BioEssays* **40**, 1800004 (2018).

47. Bowen, A. B., Bourke, A. M., Hiester, B. G., Hanus, C. & Kennedy, M. J. Golgi-independent secretory trafficking through recycling endosomes in neuronal dendrites and spines. *eLife* **6**, e27362 (2017).

48. Aridor, M. & Fish, K. N. Selective Targeting of ER Exit Sites Supports Axon Development. *Traffic* **10**, 1669–1684 (2009).

49. Gorur, A. *et al.* COPII-coated membranes function as transport carriers of intracellular procollagen I. *J. Cell Biol.* **216**, 1745–1759 (2017).

50. Hirata, Y., Matsui, Y., Wada, I. & Hosokawa, N. Endoplasmic reticulum-to-Golgi trafficking of procollagen III via conventional vesicular and tubular carriers. *Mol Biol Cell* **33**, ar21 (2022).

51. McCaughey, J., Stevenson, N. L., Cross, S. & Stephens, D. J. ER-to-Golgi trafficking of procollagen in the absence of large carriers. *J. Cell Biol.* (2018) doi:10.1083/jcb.201806035.

52. Raote, I. *et al.* TANGO1 builds a machine for collagen export by recruiting and spatially organizing COPII, tethers and membranes. *Elife* **7**, (2018).

53. Phuyal, S. & Farhan, H. Want to leave the ER? We offer vesicles, tubules, and tunnels. *J Cell Biol* **220**, e202104062 (2021).

54. Raote, I. & Malhotra, V. Protein transport by vesicles and tunnels. *J Cell Biol* **218**, 737–739 (2019).

55. Ma, W. & Goldberg, J. TANGO1/cTAGE5 receptor as a polyvalent template for assembly of large COPII coats. *PNAS* **113**, 10061–10066 (2016).

56. Saito, K. *et al.* TANGO1 facilitates cargo loading at endoplasmic reticulum exit sites. *Cell* **136**, 891–902 (2009).

57. Saito, K. *et al.* cTAGE5 mediates collagen secretion through interaction with TANGO1 at endoplasmic reticulum exit sites. *Mol. Biol. Cell* **22**, 2301–2308 (2011).

58. Venditti, R. *et al.* Sedlin controls the ER export of procollagen by regulating the Sar1 cycle. *Science* **337**, 1668–1672 (2012).

59. Fromme, J. C. *et al.* The genetic basis of a craniofacial disease provides insight into COPII coat assembly. *Dev. Cell* **13**, 623–634 (2007).

60. Boyadjiev, S. A. *et al.* Cranio-lenticulo-sutural dysplasia is caused by a SEC23A mutation leading to abnormal endoplasmic-reticulum-to-Golgi trafficking. *Nat. Genet.* **38**, 1192–1197 (2006).

61. Kim, S.-D. *et al.* The [corrected] SEC23-SEC31 [corrected] interface plays critical role for export of procollagen from the endoplasmic reticulum. *J. Biol. Chem.* **287**, 10134–10144 (2012).

62. Mastronarde, D. N. & Held, S. R. Automated tilt series alignment and tomographic reconstruction in IMOD. *J. Struct. Biol.* **197**, 102–113 (2017).

63. Zheng, S. *et al.* AreTomo: An integrated software package for automated marker-free, motion-corrected cryo-electron tomographic alignment and reconstruction. *Journal of Structural Biology: X* **6**, 100068 (2022).

64. Chaillet, M. L. *et al.* Extensive Angular Sampling Enables the Sensitive Localization of Macromolecules in Electron Tomograms. *Int J Mol Sci* **24**, 13375 (2023).

65. Ermel, U. H., Arghittu, S. M. & Frangakis, A. S. ArtiaX: An electron tomography toolbox for the interactive handling of sub-tomograms in UCSF ChimeraX. *Protein Sci* **31**, e4472 (2022).

66. Zivanov, J. *et al.* A Bayesian approach to single-particle electron cryo-tomography in RELION-4.0. *Elife* **11**, e83724 (2022).

67. Lamm, L. *et al.* MemBrain v2: an end-to-end tool for the analysis of membranes in cryo-electron tomography. 2024.01.05.574336 Preprint at https://doi.org/10.1101/2024.01.05.574336 (2024).

68. Wiedemann, S. & Heckel, R. A deep learning method for simultaneous denoising and missing wedge reconstruction in cryogenic electron tomography. *Nat Commun* **15**, 8255 (2024).

69. Pintilie, G. D., Zhang, J., Goddard, T. D., Chiu, W. & Gossard, D. C. Quantitative analysis of cryo-EM density map segmentation by watershed and scale-space filtering, and fitting of structures by alignment to regions. *J Struct Biol* **170**, 427–438 (2010).

70. Sullivan, C. B. & Kaszynski, A. A. PyVista: 3D plotting and mesh analysis through a streamlined interface for the Visualization Toolkit (VTK). *Journal of Open Source Software* **4**, 1450 (2019).

71. Waskom, M. L. seaborn: statistical data visualization. *Journal of Open Source Software* **6**, 3021 (2021).

72. Hunter, J. D. Matplotlib: A 2D Graphics Environment. *Computing in Science & Engineering* **9**, 90–95 (2007).

73. Virtanen, P. *et al.* SciPy 1.0: fundamental algorithms for scientific computing in Python. *Nat Methods* **17**, 261–272 (2020).